The thermal state of molecular clouds in the Galactic center: evidence for non-photon-driven heating[*,**]

Y. Ao[1,2], C. Henkel[1,3], K. M. Menten[1], M. A. Requena-Torres[1], T. Stanke[4], R. Mauersberger[5], S. Aalto[6], S. Mühle[7], and J. Mangum[8]

[1] Max-Planck-Institut für Radioastronomie, Auf dem Hügel 69, 53121 Bonn, Germany
    e-mail: ypao@mpifr-bonn.mpg.de
[2] Purple Mountain Observatory, Chinese Academy of Sciences, 210008 Nanjing, PR China
[3] Astron. Dept., King Abdulaziz University, PO Box 80203, Jeddah, Saudi Arabia
[4] ESO, Karl-Schwarzschild Strasse 2, 85748 Garching bei München, Germany
[5] Joint ALMA Observatory, Av. Alonso de Córdova 3107, Vitacura, Santiago, Chile
[6] Department of Earth and Space Sciences, Chalmers University of Technology, Onsala Observatory, 439 94 Onsala, Sweden
[7] Argelander-Institut für Astronomie, Universität Bonn, Auf dem Hügel 71, 53121 Bonn, Germany
[8] National Radio Astronomy Observatory, 520 Edgemont Rd., Charlottesville, VA, 22903, USA

ABSTRACT

We used the Atacama Pathfinder Experiment (APEX) 12 m telescope to observe the $J_{K_A K_c} = 3_{03} \rightarrow 2_{02}$, $3_{22} \rightarrow 2_{21}$, and $3_{21} \rightarrow 2_{20}$ transitions of para-H_2CO at 218 GHz simultaneously to determine kinetic temperatures of the dense gas in the central molecular zone (CMZ) of our Galaxy. The map extends over approximately $40' \times 8'$ ($\sim100 \times 20$ pc^2) along the Galactic plane with a linear resolution of 1.2 pc. The strongest of the three lines, the H_2CO ($3_{03} \rightarrow 2_{02}$) transition, is found to be widespread, and its emission shows a spatial distribution similar to ammonia. The relative abundance of para-H_2CO is $0.5-1.2 \times 10^{-9}$, which is consistent with results from lower frequency H_2CO absorption lines. Derived gas kinetic temperatures for individual molecular clouds range from 50 K to values in excess of 100 K. While a systematic trend toward (decreasing) kinetic temperature versus (increasing) angular distance from the Galactic center (GC) is not found, the clouds with highest temperature ($T_{kin} > 100$ K) are all located near the nucleus. For the molecular gas outside the dense clouds, the average kinetic temperature is 65 ± 10 K. The high temperatures of molecular clouds on large scales in the GC region may be driven by turbulent energy dissipation and/or cosmic-rays instead of photons. Such a non-photon-driven thermal state of the molecular gas provides an excellent template for the more distant vigorous starbursts found in ultraluminous infrared galaxies (ULIRGs).

Key words. Galaxy: center – ISM: clouds – ISM: molecules – radio lines: ISM

1. Introduction

The Galactic center (GC) region is the closest galaxy core. It is characterized by a high concentration of molecular gas located in the innermost few hundred parsec of the Milky Way, the central molecular zone (CMZ; Morris & Serabyn 1996), and by extreme conditions like high mass densities, large velocity dispersions, strong tidal forces, and strong magnetic fields. Therefore it is a unique laboratory for studying molecular gas in an environment that is quite different from that of the Milky Way's disk. For a general understanding of the physics involved in galactic cores, measurements of basic physical parameters, such as molecular gas density and gas kinetic temperature, are indispensable.

In local dark clouds, gas temperatures can be constrained by observations of the $J = 1 \rightarrow 0$ transition of CO, both because this transition is opaque and easily thermalized and because the emission even fills the beam of a single-dish telescope. At a distance of 8 kpc (Reid 1993), however, the beam filling factor of CO $J = 1 \rightarrow 0$ emission is unknown, and the GC clouds may also be affected by self-absorption. Analysis of multilevel studies of

commonly observed linear molecules like CO, HCN, or HCO$^+$ suffers from a coupled sensitivity to the kinetic temperature and gas density, making an observed line ratio consistent with both a high density at a low temperature and a low density at a high temperature. The metastable inversion lines of the symmetric top molecule ammonia (NH$_3$) are frequently used as a galactic standard cloud thermometer (Walmsley & Ungerechts 1983; Danby et al. 1988). Radiative transitions between K-ladders of NH$_3$ are forbidden, and therefore the relative populations[1] depend on the kinetic temperature of the molecular gas rather than its density. However, the fractional abundance of NH$_3$ varies between 10^{-5} in hot cores and 10^{-8} in dark clouds (e.g. Benson & Myers 1983; Mauersberger et al. 1987). Furthermore, NH$_3$ is extremely affected by a high UV flux and tends to show a characteristic "concave" shape in rotation diagrams, either caused by a variety of layers with different temperatures (e.g., due to shocks) or by the specifics of the collision rates. Symmetric top molecules such as CH$_3$C$_2$H and CH$_3$CN are not widespread and their emission is very faint (Bally et al. 1987; Nummelin et al. 1998). Therefore we should look for a *widespread* symmetric or slightly asymmetric top molecule that is more favorable for

---

[1] NH$_3$ energy levels have quantum numbers (J,K), where J denotes the total angular momentum and K its projection on the molecule's axis. For metastable levels, $J = K$.
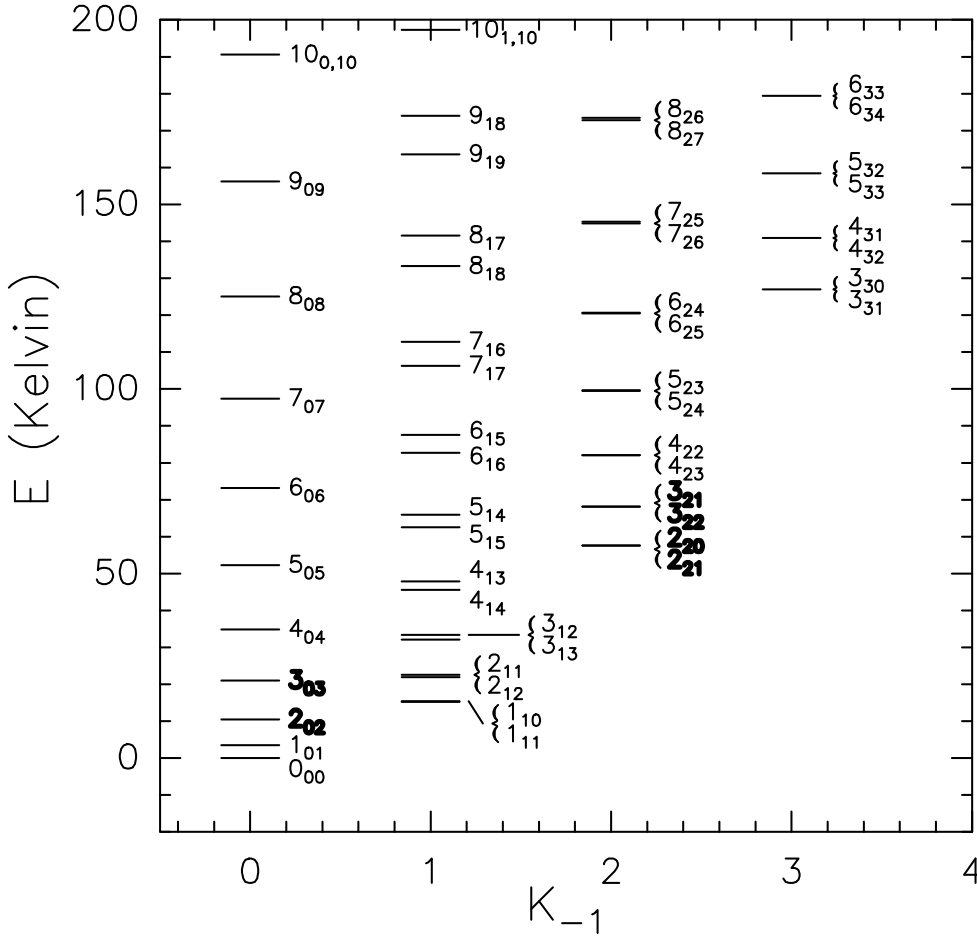
Fig. 1. H_2CO energy-level diagram up to 200 K. The H_2CO 218 GHz transitions observed in this paper are shown in bold.

spectroscopic studies to derive the kinetic temperature of the entire molecular gas.

Formaldehyde (H_2CO) is such a molecule. It is truly ubiquitous. Wootten et al. (1978) suggested that fractional H_2CO abundances decrease with increasing density of the gas in star forming regions of the Galactic disk. However, this may be due instead to decreasing volume filling factors with increasing density (e.g., Mundy et al. 1987). Unlike for NH_3, variations in the fractional abundance of H_2CO rarely exceed one order of magnitude (Johnstone et al. 2003). To give an example: the H_2CO abundance is the same in the hot core and in the compact ridge of the Orion nebula, whereas the NH_3 hot core abundance surpasses that of the ridge by about two orders of magnitude (Caselli et al. 1993; Mangum et al. 1993). We also note that for the starburst galaxy M 82, $T_{kin}(NH_3) \sim 60$ K, while for the bulk of the molecular gas $T_{kin}(H_2CO) \sim 200$ K (Weiß et al. 2001; Mauersberger et al. 2003; Mühle et al. 2007).

The relative populations of the K_a ladders of H_2CO (see Fig. 1 for an energy level diagram) are almost exclusively determined by collisional processes (Mangum & Wootten 1993). Therefore, line ratios involving different K_a ladders of one of the subspecies, either ortho- or para-H_2CO, are good tracers of the kinetic temperature (Mangum & Wootten 1993; Mühle et al. 2007). The energy levels above the ground (para)-H_2CO state are 10.5 and 21.0 K for the lower and upper states of H_2CO ($3_{03} \rightarrow 2_{02}$), and 57.6 and 68.1 K for H_2CO ($3_{21} \rightarrow 2_{20}$) and ($3_{22} \rightarrow 2_{21}$) (see Fig. 1 for all H_2CO energy levels under 200 K). Therefore, the line ratios are sensitive to gas kinetic temperatures less than 100 K, and the uncertainty in gas temperature is relatively small for a measured line ratio at $T_{kin} < 100$ K (also

see Mangum & Wootten 1993) in the case of optically thin H_2CO emission. At higher temperatures, the H_2CO 218 GHz transitions are less ideal because small changes in the ratios yield significant changes in T_{kin}, so that the H_2CO $J = 5-4$ transitions at ~364 GHz are then becoming better tracers (Mangum & Wootten 1993). The $J_{K_A K_c} = 3_{03} \rightarrow 2_{02}$, $3_{22} \rightarrow 2_{21}$, and $3_{21} \rightarrow 2_{20}$ transitions of para-H_2CO stand out by being close in frequency. With rest frequencies of 218.222, 218.475, and 218.760 GHz, respectively, all three lines can be measured simultaneously by employing a bandwidth of 1 GHz. In this way, the inter-ladder line ratios H_2CO $3_{22} \rightarrow 2_{21}/3_{03} \rightarrow 2_{02}$ and $3_{21} \rightarrow 2_{20}/3_{03} \rightarrow 2_{02}$, are free of uncertainties related to pointing accuracy, calibration errors, and different beam widths. In this paper, we therefore present observations of the H_2CO line triplet at 218 GHz to study the gas kinetic temperatures of Galactic center clouds.

2. Observations and data reduction

Simultaneous measurements of the $J_{K_A K_c} = 3_{03} \rightarrow 2_{02}$, $3_{22} \rightarrow 2_{21}$, and $3_{21} \rightarrow 2_{20}$ transitions of para-H_2CO (see Sect. 1 and Fig. 1) were obtained with the Atacama Pathfinder Experiment (APEX[2], Güsten et al. 2006) 12 m telescope located on Chajnantor (Chile) between 2010 April and 2010 June. We used the APEX-1 receiver, operating at 211−270 GHz, which employs a superconductor-insulator-superconductor (SIS) mixer

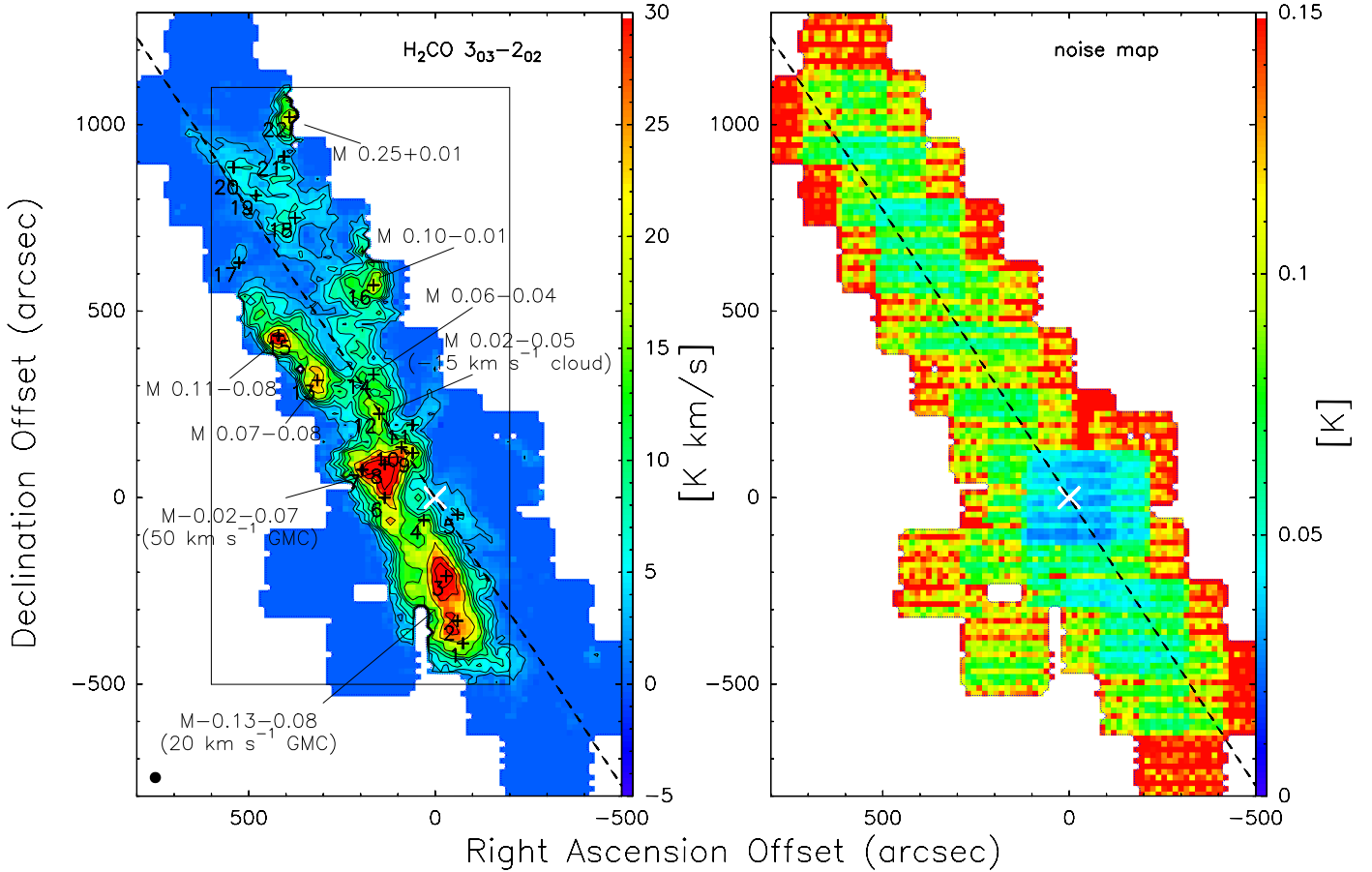**Fig. 2.** H_2CO ($3_{03} \rightarrow 2_{02}$) integrated intensity map (left) and the noise map (right) observed with the APEX in the GC. *Left:* black contour levels for the molecular line emission (on a T_A^* scale) are $-3, 3, 6, 9, 12, 15, 20, 30, 40, 50\ \sigma$ ($1\sigma = 0.72$ K km s^{-1}). The black rectangle shows a smaller region where most of the molecular line emission is detected. The molecular cloud labels with M followed by the galactic coordinates are adopted from Güsten et al. (1981). The wedge at the side shows the intensity range of the line emission on a T_A^* scale. The beam size of 30″ is shown in the bottom-left corner. *Right:* noise map across the region. The wedge at the side shows the range of noise on a T_A^* scale at a velocity resolution of 2 km s^{-1}. The spectra presented in Fig. B.1 are shown as the plus symbols with numbers. Sgr A* is the reference position and shown as a white cross symbol. The dashed line marks the Galactic plane through Sgr A*.

with a typical sideband rejection >10 dB. As backends we used a fast fourier transform Spectrometer (FFTS, Klein et al. 2006), which consists of two units with a bandwidth of 1 GHz each and a channel separation of 244 kHz. The full-width-at-half-maximum (FWHM) beam size was approximately 30″ in the observed frequency range and the typical pointing error was ∼3″. The main beam efficiency and the forward efficiency were 0.75 and 0.97, respectively.

We used the on-the-fly observing mode measuring 4′ × 4′ maps in steps of 9″ in both right ascension and declination, 0.8 s integration time per position, and one OFF position measurement after every two map rows, i.e., after about one minute of observing time. The surveyed area is 302 square arcmin and its dimension is roughly 40′ × 8′ along the Galactic plane. The total observing time was about 41 h.

The data were reduced with the CLASS software[3]. We first excluded data with a high noise level due to distorted baselines. The spectra were resampled in steps of 15″ and smoothed to a velocity resolution of 2 km s^{-1}. The final maps comprise 4825 points, corresponding to 4825 spectra for each transition. To optimize signal-to-noise ratios (S/N) of integrated intensity and channel maps, we had to determine the valid velocity ranges

---

[3] http://www.iram.fr/IRAMFR/GILDAS

for the spectra, especially for those cases where the lines were weak. To avoid noise from channels without significant emission, we first created a high S/N spectrum by smoothing all spectra within a 60″ × 60″ box to obtain a masking spectrum, for which 1 and 0 were assigned for the channels with S/N higher and lower than 5, respectively. Different line windows were automatically deteremined to cover the emission from different positions, and the baseline was removed before creating the masking spectrum. Then, the final spectra were created by multiplying the raw spectrum by the masking spectrum. Because all lines were observed simultaneously and because the H_2CO ($3_{03} \rightarrow 2_{02}$) data have the best S/N, the masking spectrum from this data set has also been applied to the other transitions by assuming the same velocity ranges for the emission from these transitions (for the details of this technique, see Dame et al. 2001; Dame 2011).

3. Results

3.1. General characteristics of the molecular gas

For the first time, observations of the triple transitions of H_2CO at 218 GHz have been performed in a large area of the GC. Fig. 2 (left panel) shows the extended line emission from the H_2CO ($3_{03} \rightarrow 2_{02}$) transition. Molecular gas, revealed by
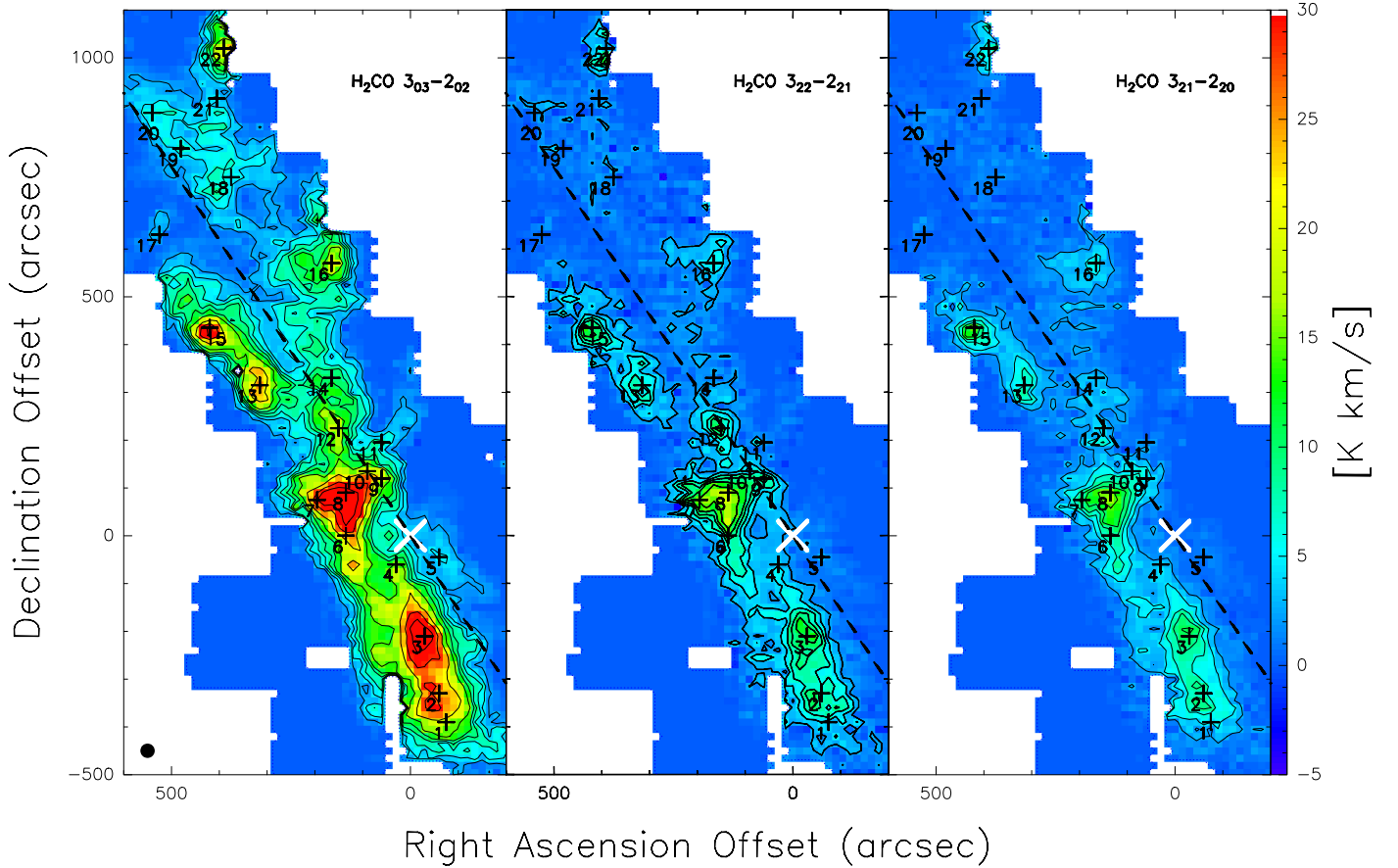
Fig. 3. Integrated intensity maps for the different transitions observed in the GC. The shown region corresponds to the rectangle (black solid line) in Fig. 2 (*left*). Black contour levels for the molecular line emission (on a T_A^* scale) are $-3, 3, 6, 9, 12, 15, 20, 30, 40, 50\,\sigma$ ($1\sigma = 0.72$ K km s^{-1}). The wedge at the side shows the intensity range of the line emission on a T_A^* scale. The beam size is shown at the bottom-left corner of the *left panel*. The dashed line marks the Galactic plane through Sgr A*.

H_2CO ($3_{03} \rightarrow 2_{02}$), shows a similar spatial distribution as ammonia (Güsten et al. 1981). All prominent features identified in ammonia, e.g., the clouds M-0.13−0.08 and M-0.02−0.07 (the molecular clouds labeled with M followed by the galactic coordinates are identified by Güsten et al. 1981), are clearly detected in H_2CO ($3_{03} \rightarrow 2_{02}$), and labeled in the figure. A map providing the noise level of the full region is also presented in Fig. 2 (right panel). The median noise value for the 4825 spectra is about 0.1 K (T_A^*) at a velocity resolution of 2 km s^{-1}. In the regions of interest where the line emission is strong, the noise level is ~0.08 K (T_A^*). To show the line emission in more detail, we also present integrated intensity maps (Fig. 3), as well as channel maps (see Sect. 3.3), for all transitions in a zoomed region in Fig. 2 (left panel). The distribution of the velocity integrated line emission of the observed three transitions is quite similar except that the weaker two H_2CO transitions are not detected in some of the regions where the $3_{03} \rightarrow 2_{02}$ transition is still observed.

3.2. Individual spectral lines

Spectra from some positions of interest are shown in Fig. B.1 with overlaid Gaussian fit profiles, and their locations are marked in Fig. 2 (left panel). To achieve better S/N, we averaged the spectra within a 30″ × 30″ area to create a new spectrum for each transition. All transitions from a given position are presented in the same panel of Fig. B.1 but with different

offsets along the y-axis. For those positions with clear detections of H_2CO $3_{22} \rightarrow 2_{21}$ and $3_{21} \rightarrow 2_{20}$, line parameters are listed in Table A.1, where integrated intensity, $\int T_{mb} dv$, peak main beam brightness temperature, T_{mb}, local standard of rest (LSR) velocity, V, and FWHM line width, $\Delta V_{1/2}$, were obtained from Gaussian fits. In most cases, only one component is needed for the Gaussian fits except in the case of H_2CO ($3_{22} \rightarrow 2_{21}$). This line is displaced from the $CH_3OH(4_{22} \rightarrow 3_{12})$ transition by only 49 km s^{-1}, and we therefore have applied in this case two component Gaussian fits.

In the central nuclear region, line emission is too weak to be detected with sufficient S/N, while H_2CO ($3_{03} \rightarrow 2_{02}$) emission is detected southwest, ~3 pc away from Sgr A*, showing the broad weak line profile belonging to P5 ($-60″$, $-45″$) in Fig. B.1.

The line parameters obtained from Gaussian fits do not show many peculiarities when one inspects the central velocities and line widths in Table A.1, as well as the line profiles in Fig. B.1. Sometimes, however, there are two velocity components, e.g., at offset positions P9 (60″, 120″) and P12 (150″, 225″) with respect to the Galactic center, and the number of components for their Gaussian fits had to be doubled. In particular, for the 44 km s^{-1} component of P12, the H_2CO ($3_{22} \rightarrow 2_{21}$) integrated intensity seems to be significantly larger than that of H_2CO ($3_{21} \rightarrow 2_{20}$), because the H_2CO ($3_{22} \rightarrow 2_{21}$) transition is blended by the emission from $CH_3OH(4_{22} \rightarrow 3_{12})$ at 218.440 GHz.
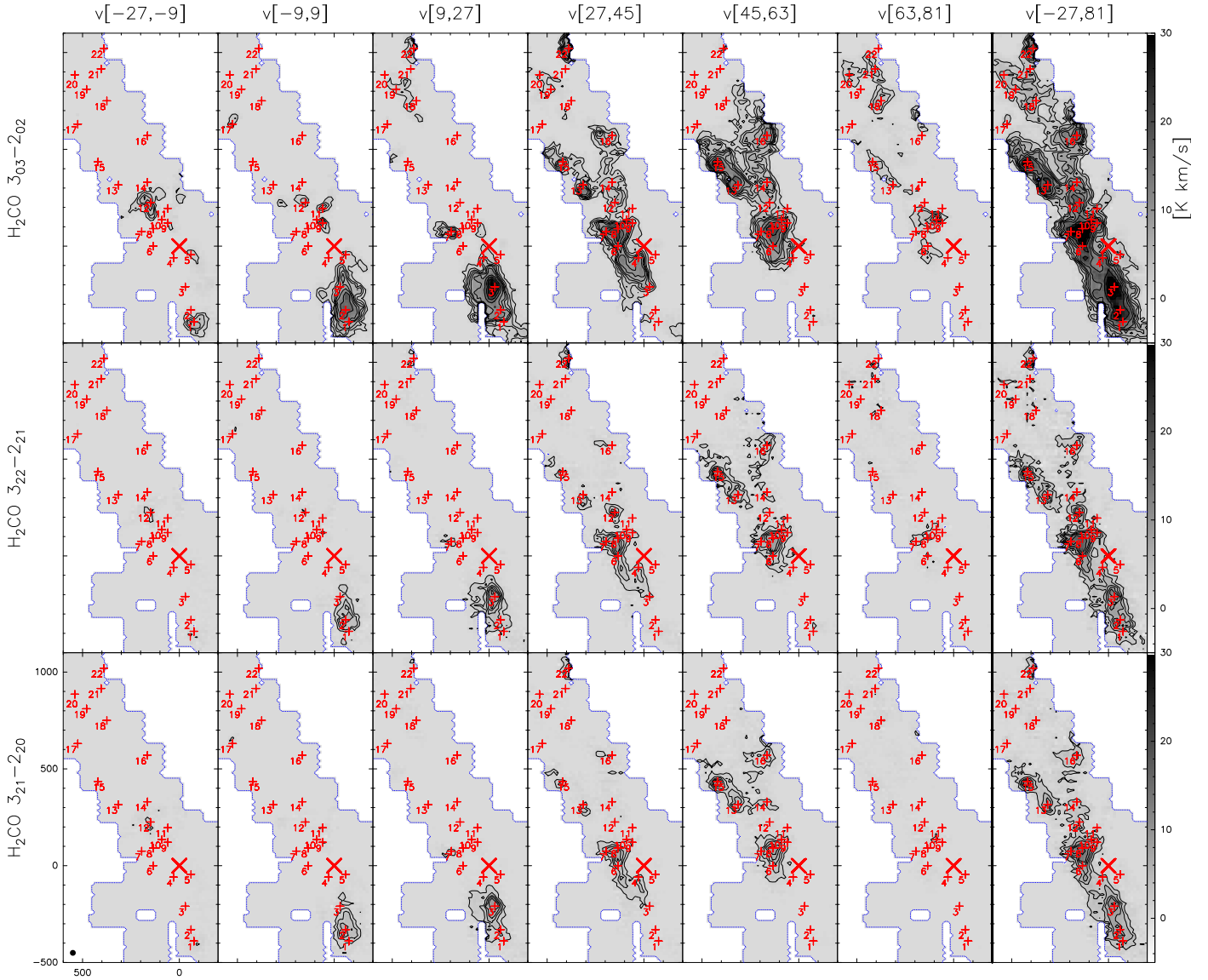
Fig. 4. Selected velocity-integrated maps for the different transitions observed in the GC. Black contour levels for the molecular line emission (on a T_A^* scale) are $-3, 3, 6, 9, 12, 15, 20, 30, 40, 50, 70\sigma$ ($1\sigma = 0.48$ K km s^{-1}) for the first six columns, and $-3, 3, 6, 9, 12, 15, 20, 30, 40, 50\sigma$ ($1\sigma = 0.72$ K km s^{-1}) for the last column, respectively. The wedges at the sides show the intensity scale of the line emission on a T_A^* scale.

3.3. Molecular line data cube

In Fig. 4, channel maps with velocity steps of 18 km s^{-1} are presented, allowing us to clearly separate the components based on both their positions and velocities. The total integrated intensity maps are also shown for comparison in the panels on the right-hand side. Channel maps in steps of 2 km s^{-1} are presented in the Appendix (Figs. B.2−B.4) to show more detail.

We choose the H$_2$CO ($3_{03} \rightarrow 2_{02}$) data to describe the individual molecular concentrations. H$_2$CO $3_{03} \rightarrow 2_{02}$ emission mainly ranges from -27 to 81 km s^{-1}. In the velocity range $[-27,-9]$, there are two prominent features, the -15 km s^{-1} cloud M 0.02−0.05 at P12, and the southernmost cloud at P1. The latter is part of the 20 km s^{-1} cloud M-0.13−0.08. There is also weak H$_2$CO $3_{03} \rightarrow 2_{02}$ emission at P5 close to Sgr A*, which traces the southwestern lobe of the circumnuclear disk (CND).

Within the velocity range $[-9,9]$, the bulk of the 20 km s^{-1} cloud appears in the south and its size is about 7 pc × 15 pc. There are three small cores at P9, P11, and P12 with sizes of ~1

to 2 pc in the northeast and one small cores at P17 even farther away from Sgr A*. The peak of the 20 km s^{-1} cloud moves from south ($-75''$, $-390''$) relative to the Galactic center to north ($-30''$, $-210''$), increasing the velocity from -27 to $+27$ km s^{-1}.

Within the velocity range $[9,27]$, there is a dense concentration at P7 with a size of ~2.7 pc × 5.4 pc. Extended weak emission is detected around P19 in an irregular morphology with a size of ~2 pc × 9 pc. The northernmost core, M 0.25+0.01, begins to appear at P22. This concentration is not fully covered by our observations.

In the velocity range $[27,63]$, the line emission shows a complex morphology. The prominent features are the 50 km s^{-1} cloud M-0.02−0.07 around P6, P7, and P8, two compact concentrations M 0.07−0.08 at P13 and M 0.11−0.08 at P15, an extended region of weak emission associated with M 0.06−0.04 around P12 and P14, a concentration M 0.10−0.01 around P16, and the northernmost core M 0.25 + 0.01 at P22. In the velocity range $[27,45]$, the gas in the southeast close to Sgr A* appears to connect the 20 km s^{-1} and 50 km s^{-1} clouds.

In the extreme velocity range [63,81], the 50 km s^{-1} cloud moves to the west by ~60″ with respect to [27,63], and peaks at P10, the edge of the cloud. In addition to features identified in the previous velocity ranges, there are three clumps around P18, P20, and P21, with sizes of about 3 pc × 6 pc.

4. Discussion

4.1. Formaldehyde column density and abundance

In the following we derive H$_2$CO column densities and abundances. Assuming the line emission is optically thin and the contribution from the cosmic microwave background is negligible, the H$_2$CO column density, $N(J_{K_A K_c})$, in an upper state $J_{K_A K_c}$ can be obtained by

$$N(J_{K_A K_c}) = \frac{3k}{8\pi^3 \nu S \mu^2} \frac{h\nu/kT_{ex}}{e^{h\nu/kT_{ex}} - 1} \int T_{mb}\, dv, \qquad (1)$$

(for the equations in this subsection, see Mangum & Shirley 2008[4]), where h is Planck's constant, k denotes Boltzmann's constant, μ is the dipole moment, ν the frequency of the transition, T_{ex} the excitation temperature, S the line strength, T_{mb} the main beam brightness temperature, and $\int T_{mb}\, dv$ the integrated line intensity for the transition $J_{K_A K_c} \to (J-1)_{K_A K_c - 1}$. H$_2$CO is a slightly asymmetric top molecule, and its line strength, S, can be approximately calculated as for a symmetric top molecule by

$$S = \frac{J^2 - K_A^2}{J(2J + 1)}. \qquad (2)$$

The total column density, N_{total}, is related to the column density, $N(J_{K_A K_c})$, in the upper state $J_{K_A K_c}$ by

$$\frac{N_{total}}{N(J_{K_A K_c})} = \frac{Z}{g_J g_K g_I} \exp\left(\frac{E(J_{K_A K_c})}{kT_{ex}}\right), \qquad (3)$$

where $g_J (= 2J + 1)$ is the rotational degeneracy, g_K marks the K degeneracy, g_I the nuclear spin degeneracy, $E(J_{K_A K_c})$ the energy of state $J_{K_A K_c}$ above the ground level, and Z the partition function. The partition function Z can be calculated by

$$Z = \sum_{J=0}^{\infty} \sum_{K_A=0}^{J} \sum_{K_c=J-K_A}^{J-K_A+1, K_c \leq J} g_J g_K g_I \exp\left(-\frac{E(J_{K_A K_{rmc}})}{kT_{ex}}\right). \qquad (4)$$

For para-H$_2$CO, $g_K = 1$, $g_I = 1$, and K_a can only be even. Here we include 41 levels with energies above ground state up to 286 K and assume the same excitation temperatures for all transitions (i.e., local thermodynamical equilibrium, LTE) to estimate the partition function. Substituting units and parameters for H$_2$CO ($3_{03} \to 2_{02}$) in Equation (3), and assuming an excitation temperature of 10 K, the total para-H$_2$CO column density, N_{total}, is

$$N_{total} = 1.32 \times 10^{12} \int T_{mb}(3_{03} \to 2_{02})\, dv\, \text{cm}^{-2}, \qquad (5)$$

where the integrated line intensity, $\int T_{mb}(3_{03} \to 2_{02})\, dv$, is in units of K km s^{-1}.

For the Sgr A* complex with a size of 30 pc in diameter, corresponding to ~ 13 arcmin, the estimated molecular gas mass is

---

[4] https://safe.nrao.edu/wiki/pub/Main/MolInfo/column-density-calculation.pdf

~0.4 × 10^6 $M_\odot$ (Kim et al. 2002), yielding an average H$_2$ column density of 2.6 × 10^{22} cm^{-2}. In this region, 2161 formaldehyde spectra were obtained with a spacing of 15″, and the average spectrum has an integrated intensity of 10.5 K km s^{-1} on a T_{mb} scale. The derived averaged para-H$_2$CO column density is 1.4 × 10^{13} cm^{-2} assuming an excitation temperature of 10 K. Adjusting the excitation temperature in the range of 5 to 40 K, the resulting total para-H$_2$CO column density will decrease with increasing T_{ex} from 5 K to around 14 K, because with increasing T_{ex} the populations of the $J = 2$ and 3 states become more dominant. Beyond $T_{ex} = 14$ K the resulting column densities will increase with excitation temperature because then also the $J > 3$ levels will be populated. For $T_{kin} \lesssim 100$ K (see Sect. 4.3 for large velocity gradient (LVG) modeling), T_{ex} values $\gtrsim 40$ K require densities $\gtrsim 10^6$ cm^{-3}, which are unrealistically high on a large spatial scale (e.g., Güsten & Henkel 1983). Therefore higher T_{ex} values can probably be excluded and the corresponding averaged para-H$_2$CO column density can be constrained to (1.3−3.1) × 10^{13} cm^{-2}. The resulting para-H$_2$CO abundance is (0.5−1.2) × 10^{-9}. This abundance agrees with the values found by Güsten & Henkel (1983) and Zylka et al. (1992), who used $K_a = 1$ ortho-formaldehyde K-doublet absorption lines to obtain H$_2$CO abundances of ~10^{-10} to 2 × 10^{-9} in the Galactic center region. Thus it is reasonable to adopt two fixed limiting para-H$_2$CO abundances of 10^{-9} and 10^{-10} for the LVG analysis in Sect. 4.3.

4.2. Line ratios

In this survey, the three 218 GHz rotational transition lines of H$_2$CO are observed simultaneously at the same angular resolution, providing good data sets to derive the H$_2$CO line ratios. Before quantitatively determining gas kinetic temperatures, we first present H$_2$CO $3_{22} \to 2_{21}/3_{03} \to 2_{02}$ and $3_{21} \to 2_{20}/3_{03} \to 2_{02}$ line ratios in Fig. 5 as probes of gas temperature. The line ratio maps are derived from both channel maps and total integrated intensity maps, and the ratios are calculated by integrating channels where the H$_2$CO($3_{03} \to 2_{02}$) line emission is detected above 5 σ. Since the excitation conditions for $3_{22} \to 2_{21}/3_{03} \to 2_{02}$ and $3_{21} \to 2_{20}/3_{03} \to 2_{02}$ are very similar, these two line ratio maps should be nearly identical, and indeed the differences mainly arise from the CH$_3$OH contamination in H$_2$CO $3_{22} \to 2_{21}$.

As seen in Fig. 5, the H$_2$CO $3_{21} \to 2_{20}/3_{03} \to 2_{02}$ line ratio, with a median value of 0.23, varies significantly across the mapped region, from about 0.15 at the edge of the clouds to ~0.35 toward the 20 km s^{-1} GMC and the compact concentration M 0.11−0.08 at P15. In case of narrow one-component features, the $3_{22} \to 2_{21}/3_{03} \to 2_{02}$ ratios follow the same trend as the $3_{21} \to 2_{20}/3_{03} \to 2_{02}$ ratios. For the 20 km s^{-1} GMC, the line ratio is higher in the south than in the north in the velocity range [−9,9]. Within the velocity range [9,27], the ratio becomes higher at P3 in the north of the 20 km s^{-1} GMC. The molecular clouds around P18, P19, and P20 have two velocity components as presented in Fig. B.1, one at ~25 km s^{-1} and another at ~78 km s^{-1}, and are characterized by low line ratios as clearly shown in Fig. 5 (bottom). Higher line ratios tend to suggest higher gas kinetic temperatures and vice versa because the relative populations of the K_a ladders of H$_2$CO are almost exclusively determined by collisional processes (Mangum & Wootten 1993). To be more quantitative and to relate the line ratios to kinetic temperatures, we need to adopt LVG radiative transfer modeling, which is done in the following section.
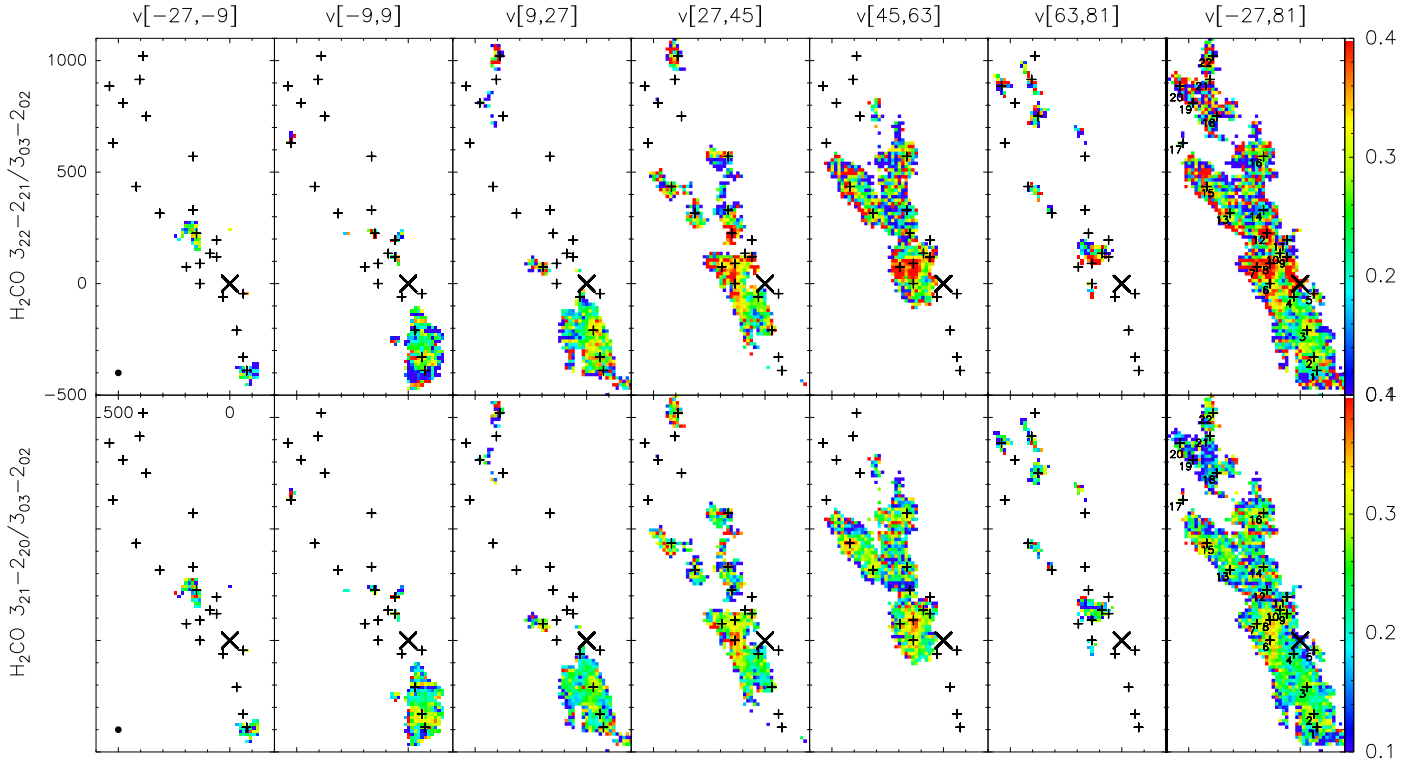
Fig. 5. $H_2CO\ 3_{22} \rightarrow 2_{21}/3_{03} \rightarrow 2_{02}$ (*top*) and $3_{21} \rightarrow 2_{20}/3_{03} \rightarrow 2_{02}$ (*bottom*) integrated intensity ratio map. Ratios are calculated when the $H_2CO\ 3_{03} \rightarrow 2_{02}$ line emission is detected above 5σ. The top and bottom rows should be nearly identical, and the difference mainly comes from the CH_3OH contamination in $H_2CO\ 3_{22} \rightarrow 2_{21}$. The wedges at the sides show the line ratios. The beam size of $30''$ is shown at the bottom-left corner. Sgr A* is the origin for the offset coordinates and shown as a cross.

4.3. Kinetic temperatures of the Galactic center clouds

To evaluate gas kinetic temperatures, we selected the positions with the Gaussian fits listed in Table A.1 (see also Fig. B.1). To investigate the gas excitation from the H_2CO line measurements, we use a one-component LVG radiative transfer model with collision rates from Green (1991) and choose a spherical cloud geometry with uniform kinetic temperature and density as described in Mangum & Wootten (1993). Dahmen et al. (1998) estimated that the velocity gradient ranges from 3 to 6 km s^{-1} pc^{-1} for Galactic center clouds. Here we adopt two fixed para-H_2CO abundances of [para-H_2CO] = 10^{-9} and 10^{-10} (see Sect. 4.1), and a velocity gradient of $(\mathrm{d}v/\mathrm{d}r) = 5$ $(\mathrm{km\,s^{-1}})\,\mathrm{pc^{-1}}$. The modeled parameter space encompasses gas temperatures, T_{kin}, from 10 to 300 K with a step size of 5 K and H_2 number densities per cm^3, $\log n_{H_2}$, from 3.0 to 7.0 with a logarithmic step size of 0.1. According to Green (1991), collisional excitation rates for a given transition are accurate to ~20%.

We first choose the $H_2CO\ 3_{22} \rightarrow 2_{21}$ and $3_{03} \rightarrow 2_{02}$ data as input parameters. Although the $3_{22} \rightarrow 2_{21}$ transition is blended with CH_3OH at a few positions, its line emission is stronger than that of $H_2CO\ 3_{21} \rightarrow 2_{20}$, and the components can be separated in all cases. This even holds for position P12 (see Sect. 3.2), where we have determined the central velocities of the two velocity components from $H_2CO\ 3_{03} \rightarrow 2_{02}$ to then carry out a four-component Gaussian fit to both $H_2CO\ 3_{03} \rightarrow 2_{02}$ and $CH_3OH\ 4_{22} \rightarrow 3_{12}$. Comparing computed line intensities and their line ratios with the corresponding observational results, we can constrain the kinetic temperature. The gas density is not well known because it is highly dependent on the adopted fractional abundance, velocity gradient, and filling factors. Here we choose

a filling factor of unity to fit the data, implying that we obtain beam averaged quantities.

In Fig. 6 (top), an example is presented to show how the parameters are constrained by the reduced χ^2 distribution of H_2CO line measurements in the T_{kin}-n parameter space. As can be seen, observed $H_2CO\ 3_{22} \rightarrow 2_{21}/3_{03} \rightarrow 2_{02}$ line ratios (the approximately horizontal lines in the diagram) are a good measure of T_{kin}, independent of density, as long as the transitions are optically thin. In contrast, the density is poorly constrained, as can be inferred by the different resulting densities for the chosen limiting fractional H_2CO abundances (in the specified case of Fig. 6, the range covers a factor of 3−4 if assuming a filling factor of unity). In Table 1, we present derived gas kinetic temperatures averaged over $30''$ boxes at the positions shown in Figs. 2 and B.1. It is worth noting that in most cases the two adopted para-H_2CO abundances, differing by a factor of 10 (Sect. 4.1), cause only a slight change of less than 10 K in kinetic temperature because the 218 GHz H_2CO transitions remain optically thin in most parameter ranges except for gas densities higher than $10^{4.6}$ cm^{-3} in the case of [para-H_2CO] = 10^{-9}. For [para-H_2CO] = 10^{-10} this limiting density is well above 10^5 and outside the plotted range of densities of Fig. 6 (top). This demonstrates that H_2CO is a good molecular thermometer and can be used to reliably determine kinetic temperatures.

Gas temperatures range from 50 K in the southern part of the 20 km s^{-1} cloud to above 100 K in the 50 km s^{-1} cloud and the molecular core of M 0.07−0.08. While a systematic trend of (decreasing) kinetic temperature versus (increasing) angular distance from the nucleus is not found, the clouds with highest temperature ($T_{\mathrm{kin}} > 100$ K) are all located near the center. To estimate the overall gas temperature on a large scale of ~90 pc,
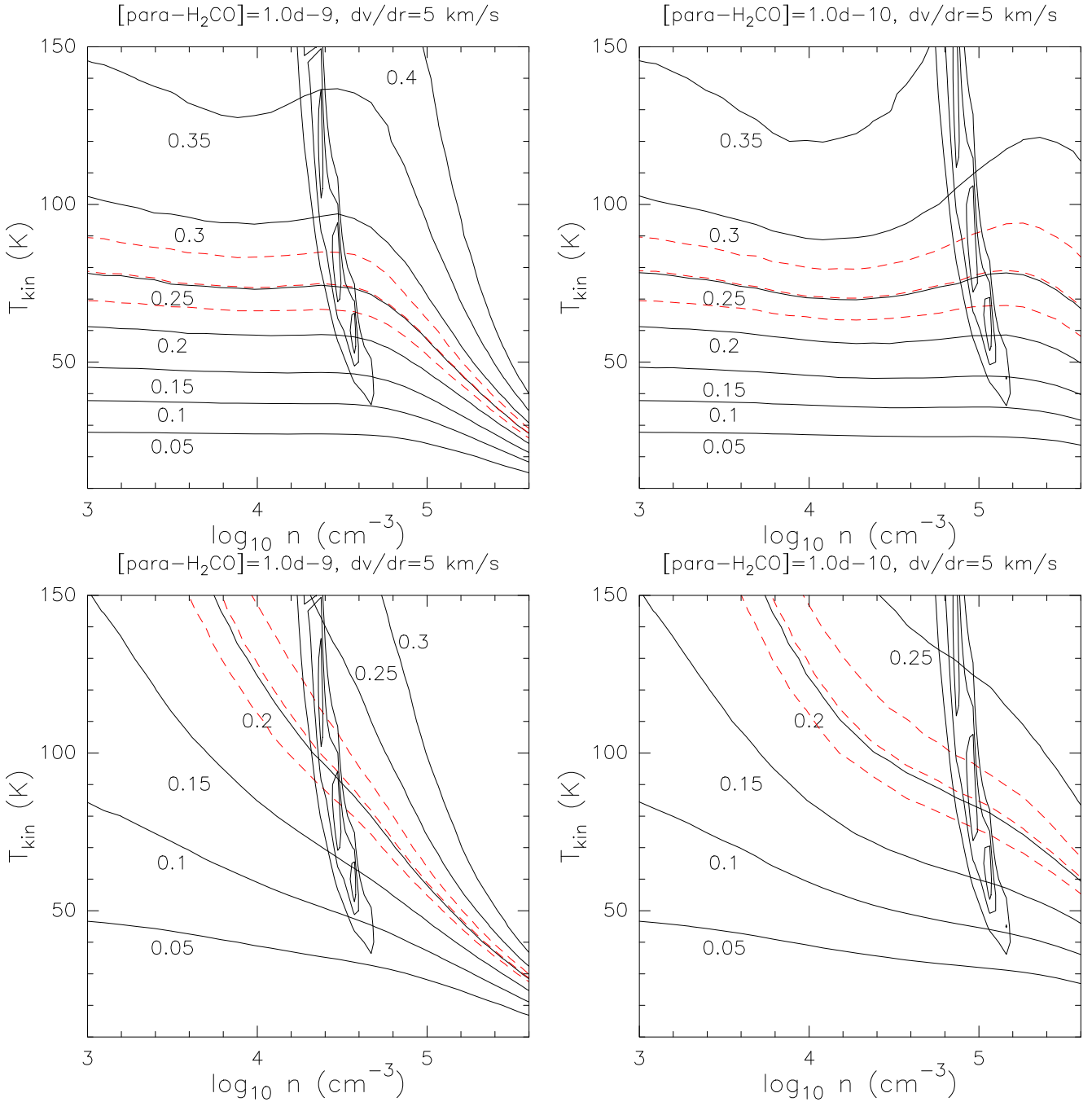
Fig. 6. Example of LVG modeling for P4. *Top:* reduced χ^2 distribution (mainly vertical contours) for a single-component LVG model fit to the H_2CO brightness temperatures (black contours, $\chi^2 = 1,2,4$), as well as H_2CO $3_{22} \to 2_{21}/3_{03} \to 2_{02}$ line ratios (mainly horizonal contours) as a function of n_{H_2} and T_{kin}. The solid lines represent the line ratios: 0.05, 0.1, 0.15, 0.2, 0.25, 0.3, 0.35, 0.4. The red dashed lines show the observed line ratio and its lower and upper limits. The para-H_2CO abundances per velocity gradient, [para-H_2CO]/(dv/dr), for the LVG models are 2×10^{-10} pc (km s^{-1})$^{-1}$ (*left*) and 2×10^{-11} pc (km s^{-1})$^{-1}$ (*right*), respectively. In the left panel the lines with a given H_2CO line ratio move downwards (lower T_{kin}) at high density because the H_2CO lines start to become saturated; this causes intensity ratios for a given T_{kin} to get closer to unity. *Bottom:* reduced χ^2 distribution for the H_2CO $3_{21} \to 2_{20}/3_{03} \to 2_{02}$ line ratios. The kinetic temperature is sensitive to the gas density so this line ratio is a less suitable thermometer.

we mask the dense clouds by clipping all the emission above 3σ in T_A^* of the H_2CO ($3_{03} \to 2_{02}$) line within a $60'' \times 60''$ box and create an averaged spectrum, yielding a gas kinetic temperature of 65 ± 10 K for more diffuse molecular gas outside of the dense cores in the GC region.

If we instead use the H_2CO $3_{21} \to 2_{20}/3_{03} \to 2_{02}$ line ratio to constrain gas properties, the kinetic temperature is somewhat more sensitive to the gas density so that this line ratio is not

quite as good as a thermometer (see Fig. 6, bottom). Therefore, we focus exclusively on the H_2CO $3_{22} \to 2_{21}/3_{03} \to 2_{02}$ line ratio to derive the gas kinetic temperature in this study.

High gas temperatures were first deduced from the metastable transitions of ammonia (Güsten et al. 1981, 1985a,b; Hüttemeister et al. 1993). Using the CO 7−6/4−3 line ratio, Kim et al. (2002) report, for the Sgr A complex, a gas kinetic temperature of 47 K on a linear scale of 30 pc. From

Table 1. H_2CO LVG results.

Position	[para-H_2CO] $= 10^{-9}$ T_{kin} (K)	[para-H_2CO] $= 10^{-10}$ T_{kin} (K)	T_{turb}[a] (K)
P1 ($-75''$, $-390''$)	50^{+10}_{-5}	55^{+15}_{-10}	107
P2 ($-69''$, $-330''$)	75^{+10}_{-10}	80^{+20}_{-10}	55
P3 ($-30''$, $-210''$)	85^{+10}_{-5}	105^{+25}_{-10}	57
P4 ($+30''$, $-60''$)	75^{+20}_{-15}	75^{+25}_{-10}	59
P6 ($+135''$, $0''$)	90^{+25}_{-10}	100^{+35}_{-15}	91
P7 ($+195''$, $75''$)	85^{+15}_{-10}	95^{+35}_{-15}	111
P8 ($+135''$, $+90''$)	190^{+60}_{-30}	>250	82
P9 ($+60''$, $+120''$/ 49 km s^{-1})	125^{+95}_{-45}	140^{+120}_{-55}	86
P9 ($+60''$, $+120''$/-4 km s^{-1})	90^{+90}_{-25}	95^{+120}_{-40}	58
P10 ($+90''$, $+135''$)	110^{+25}_{-20}	130^{+50}_{-30}	90
P12 ($+150''$, $+225''$/-11 km s^{-1})	80^{+50}_{-20}	85^{+65}_{-25}	45
P12 ($+150''$, $+225''$/44 km s^{-1})	55^{+20}_{-10}	55^{+25}_{-10}	63
P13 ($+315''$, $+315''$)	85^{+20}_{-15}	95^{+35}_{-25}	66
P14 ($+165''$, $+330''$)	55^{+20}_{-10}	55^{+20}_{-15}	38
P15 ($+420''$, $+435''$)	125^{+25}_{-25}	180^{+70}_{-55}	64
P16 ($+165''$, $+570''$)	80^{+35}_{-15}	85^{+50}_{-15}	61
P22 ($+390''$, $+1020''$)	65^{+20}_{-10}	70^{+25}_{-15}	68

Notes. A velocity gradient of 5 km s^{-1} pc^{-1}, a filling factor of unity, and the H_2CO $3_{22} \rightarrow 2_{21}/3_{03} \rightarrow 2_{02}$ line ratios averaged over $30''$ boxes were adopted in the LVG models to derive the solutions presented in Cols. 2−3. [a] The temperatures in Col. 4 are calculated with Eq. (20) with a velocity gradient of 5 km s^{-1} pc^{-1}, a typical gas density of $10^{4.5}$ cm^{-3}, and a cloud size, i.e., turbulent scale, of 5 pc.

mm- and submm-line spectroscopy, Oka et al. (2011) deduced temperatures of at least 63 K in the CND. The 20 km s^{-1} and 50 km s^{-1} clouds were studied by Güsten et al. (1981, 1985a,b) with species like NH$_3$ and CH$_3$CN and by Mauersberger et al. (1986) in the $(J,K) = (7,7)$ metastable inversion line of ammonia, yielding gas temperatures in the range 80−100 K. These results are roughly consistent with the temperatures derived by us from H_2CO. We emphasize, however, that ammonia may be more affected than H_2CO by a peculiar molecule specific chemistry and that the degeneracy between high T_{kin} and low $n(H_2)$ or vice versa is difficult to overcome for the mm- and submm-transitions from linear molecules.

A high gas temperature will affect the Jeans masses of dense cores (e.g., for a molecular cloud, its Jeans' mass is $M_J = (\frac{5 k T_{kin}}{G \mu 2 m_p})^{1.5} (\frac{4\pi}{3})^{-0.5} \rho^{-0.5} = 1.25 (\frac{T_{kin}}{10 K})^{1.5} (\frac{n}{10^5 cm^{-3}})^{-0.5} M_\odot$, where n is volume density and T_{kin} is gas kinetic temperature. $M_J \sim 1.2 M_\odot$ for $T_{kin} = 10$ K and $n = 10^5$ cm^{-3}, and $14−39 M_\odot$ for $T_{kin} = 50−100$ K and $n = 10^5$ cm^{-3}), and may affect the initial mass function (IMF) of star formation, resulting in a top-heavy IMF in the Galactic center region (Klessen et al. 2007). Indeed, Alexander et al. (2007) suggest a top-heavy IMF to explain the observed ring of massive stars orbiting about 0.1 pc around the Galactic center. However, Bartko et al. (2010) do not find evidence of a top-heavy IMF at distances beyond $12''$ from Sgr A*. Higher densities in the GC clouds with respect to those in the spiral arms due to a higher stellar density and strong tidal forces may lead to lower Jeans masses and may thus counteract the effect of higher temperatures.

4.4. Heating mechanisms in the GC: turbulent heating or cosmic-ray heating

What heats the dense gas to high temperatures in the GC? The four most common mechanisms for heating the gas in molecular clouds are (a) photo-electric heating in photon-dominated regions (PDRs), (b) X-ray heating (XDRs), (c) cosmic-ray heating (CRDRs), and (d) turbulent heating. In star-forming regions, gas can be heated by electrons released from normal dust grains or polycyclic aromatic hydrocarbons (PAHs). Gas and dust are thermally coupled in very dense regions ($n_{H_2} > 10^5$ cm^{-3}; e.g., Krügel & Walmsley 1984). However, the gas temperatures derived from H_2CO are much higher than the fairly uniform dust temperatures of $\sim 14−20$ K in the dense clouds of the GC (Pierce-Price et al. 2000; García-Marín et al. 2011; Molinari et al. 2011). Photons can drive such decoupling only at the very surface of irradiated clouds ($\sim$a few percent of their total molecular gas mass; see Bradford et al. 2003 and references therein). Only there might they have a chance to dissociate complex molecules, such as H_2CO, which then necessarily probe much deeper and UV-shielded gas regions where photo-electric heating of the gas is no longer dominant. Therefore, some other process(es) should exist that are efficient at directly heating the gas from outside. X-ray heating (Maloney et al. 1996), cosmic-ray heating (Güsten et al. 1981, 1985a,b; Papadopoulos 2010), and turbulent heating (Güsten et al. 1985a,b; Schulz et al. 2001; Pan & Padoan 2009) are such potential heating mechanisms.

A few other heating processes also deserve to be mentioned. Gravitational heating (Goldsmith & Langer 1978; Tielens 2005) is important during the collapse phase of molecular cloud cores. However, gravitational collapse is a temporary phase and star-forming activity, with the notable exception of Sgr B2 (not covered by our survey), is not vigorous in the clouds of the CMZ. Heating of the gas by magnetic ion-neutral slip (Scalo 1977; Goldsmith & Langer 1978) would require further observations of the ionization fraction and the magnetic fields of the molecular clouds (see, e.g., Ferriére 2009; Croker et al. 2010), which is outside the scope of this paper. In a highly turbulent environment, the effect of a magnetic field on the cloud is to decrease the dissipation of kinetic energy, i.e., turbulent heating, and to lead to a lower gas kinetic temperature. Having already mentioned

PDRs, we discuss in the following XDRs, CRDRs, and the dissipation of turbulence.

4.4.1. X-ray heating

In X-ray dominated regions (XDRs), X-rays photoionize atoms and molecules, depositing a significant fraction of the primary and secondary electron energy in heat (Maloney et al. 1996; Hollenbach & Tielens 1999). Unlike UV photons, hard X-ray photons are capable of deeply penetrating dense molecular clouds and heating large amounts of gas. The X-ray heating rate is given by

$$\Gamma_X = 1.2 \times 10^{-19} \left(\frac{n}{10^5 \, \text{cm}^{-3}} \right) \left(\frac{F_X}{\text{erg cm}^{-2} \, \text{s}^{-1}} \right)$$
$$\times \left(\frac{N}{10^{22} \, \text{cm}^{-2}} \right)^{-0.9} \text{erg cm}^{-3} \, \text{s}^{-1} \quad (6)$$

(Maloney et al. 1996), where n is gas density in units of cm^{-3}, F_X is X-ray flux density in units of erg cm^{-2} s^{-1}, and N the column density of hydrogen attenuating the X-ray flux. For the dense cores studied here, N is of the order of 10^{23} cm^{-2}. In the region associated with the Galactic center and encompassing a diameter of about 20 arcminutes, the total X-ray luminosity in the range 2 to 40 KeV (Muno et al. 2004; Koyama et al. 2007; Yuasa et al. 2008; Dogiel et al. 2010) is 6×10^{36} erg s^{-1}, yielding an X-ray flux density of 2.0×10^{-3} erg cm^{-2} s^{-1}.

The gas cooling via gas-dust interaction can be expressed as

$$\Lambda_{g-d} \sim 4 \times 10^{-33} \, n^2 \, T_{kin}^{1/2} (T_{kin} - T_d) \, \text{erg cm}^{-3} \, \text{s}^{-1} \quad (7)$$

(Tielens 2005), where T_{kin} is the gas kinetic temperature and T_d dust temperature. For a gas density range of 10^4 to 10^6 cm^{-3}, accounting for the velocity gradient, dv/dr, the line cooling is approximated well by the expression

$$\Lambda_{gas} \sim 6 \times 10^{-29} \, n^{1/2} \, T_{kin}^3 \, \text{d}v/\text{d}r \, \text{erg cm}^{-3} \, \text{s}^{-1} \quad (8)$$

(Goldsmith & Langer 1978; Goldsmith 2001; Papadopoulos 2010), where dv/dr is the velocity gradient adopted to calculate the line cooling rate in the LVG radiative transfer models. The line cooling is through rotational lines of CO, its isotopologues ^{13}CO and C^{18}O, and other species (Goldsmith 2001). If the water is highly abundant in the warm clouds of the CMZ, the line cooling from the water emission will be important, and this will lead to lower gas kinetic temperatures in this section. However, this will not drastically change our results, because water is unlikely to be that dominant. Furthermore, water vapor only affects the cooling rate and not the heating process, so that our evaluation of relative efficiencies of different heating processes is not seriously affected.

If X-ray heating dominates the heating process, the gas kinetic temperature can be estimated from the thermal equilibrium

$$\bar{\Gamma}_X = \Lambda_{g-d} + \Lambda_{gas}. \quad (9)$$

To simply solve the equation above, we set the dust temperature to $T_d = 0$ K, yielding a minimum T_{kin} value and its simple analytic solution as below

$$T_{kin} = \left(\frac{(16 \times 10^{-8} \, n^3 + 720 \, n^{0.5} \, \text{d}v/\text{d}r \, F_X \, (N/10^{23})^{-0.9})^{0.5}}{12 \, \text{d}v/\text{d}r} \right.$$
$$\left. - \frac{4 \times 10^{-4} \, n^{1.5}}{12 \, \text{d}v/\text{d}r} \right)^{2/3}. \quad (10)$$

Choosing a velocity gradient of 5 km s^{-1} pc^{-1}, and adopting the observed X-ray flux density of 2.0×10^{-3} erg cm^{-2} s^{-1}, the derived gas kinetic temperature is only 1 K. It indicates that the observed X-ray flux density cannot explain the high gas temperatures observed by formaldehyde. Peculiar conditions in the CMZ, like a potentially high water vapor abundance, enhancing cooling, or a high magnetic field inhibiting the dissipation of turbulent motion, would not help to diminish the resulting discrepancy.

To simplify this: if the X-ray flux density were about 500 times higher than the observed value and line cooling dominates the cooling process, we could derive an approximate gas temperature with

$$T_{kin} = 45 \left(\frac{n}{10^{4.5} \, \text{cm}^{-3}} \right)^{1/6} \left(\frac{\text{d}v/\text{d}r}{5 \, \text{km s}^{-1} \, \text{pc}^{-1}} \right)^{-1/3}$$
$$\times \left(\frac{F_X}{500 \times 2.0 \times 10^{-3} \, \text{erg cm}^{-2} \, \text{s}^{-1}} \right)^{1/3} \left(\frac{N}{10^{23} \, \text{cm}^{-2}} \right)^{-0.3} \text{K}. \quad (11)$$

This equation shows that T_{kin} depends weakly on the gas density, velocity gradient, column density of hydrogen attenuating the X-ray emission, and X-ray flux density. The first three parameters cannot change significantly. If X-rays really play an important role in heating the gas, an X-ray flux density, about three orders of magnitude higher than observed, is required. Such an intense X-ray radiation field may exist in some spatially confined regions. However, it cannot explain the high gas temperatures on the large spatial scales of the GC. Recent observations (e.g., Eckart et al. 2012; Nowak et al. 2012) confirm that the X-ray emission from Sgr A* shows flares, almost daily, by factors of a few to ten times over the quiescent emission level, and rarely even up to more than 100 times that level on time scales from a few minutes to a few hours. However, this is still much less than what is required to explain our observed kinetic gas temperatures.

4.4.2. Cosmic-ray heating

For the UV-shielded and mostly subsonic dense gas cores (e.g., dark clouds), cosmic-ray heating is the major heating process, and it may also play an important role in heating the gas in the GC because the cosmic-ray flux density is enhanced by the supernovae in this region. The cosmic-ray heating rate is given by

$$\Gamma_{CR} \sim 3.2 \times 10^{-28} \, n \left(\frac{\zeta_{CR}}{10^{-17} \, \text{s}^{-1}} \right) \text{erg cm}^{-3} \, \text{s}^{-1} \quad (12)$$

(Goldsmith & Langer 1978), where ζ_{CR} is the total cosmic-ray ionization rate. If the gas heating in the GC is dominated by the cosmic-ray heating, we can obtain the gas kinetic temperature from the energy balance equation

$$\Gamma_{CR} = \Lambda_{g-d} + \Lambda_{gas}. \quad (13)$$

As above in Sect. 4.4.1, we set the dust temperature to $T_d = 0$ K, yielding a minimum T_{kin} value and the following analytic solution as below

$$T_{kin} = \left(\frac{(16 \times 10^{-8} \, n^3 + 768 \, n^{0.5} \, \text{d}v/\text{d}r \, \frac{\zeta_{CR}}{10^{-17} \, \text{s}^{-1}})^{0.5}}{12 \, \text{d}v/\text{d}r} \right.$$
$$\left. - \frac{4 \times 10^{-4} \, n^{1.5}}{12 \, \text{d}v/\text{d}r} \right)^{2/3}. \quad (14)$$

Similarly, we can obtain a simple solution as below if line cooling dominates the cooling process

$$T_{\rm kin} = 6 \left(\frac{n}{10^{4.5}\,{\rm cm}^{-3}}\right)^{1/6} \left(\frac{{\rm d}v/{\rm d}r}{5\,{\rm km\,s}^{-1}\,{\rm pc}^{-1}}\right)^{-1/3}$$
$$\times \left(\frac{\zeta_{\rm CR}}{10^{-17}\,{\rm s}^{-1}}\right)^{1/3}\,{\rm K}. \tag{15}$$

If cosmic-rays are the only heating source, gas temperatures are constrained by three parameters: gas density, velocity gradient, and the cosmic-ray ionization rate. It is reasonable to adopt a gas density of $10^{4.5}$ cm^{-3} (still low enough to yield (almost) optically thin H$_2$CO $3_{03} \to 2_{02}$ emission) and a velocity gradient of 5 km s^{-1} pc^{-1} for the clouds in the GC. The poorly determined parameter is the comic-ray ionization rate. Using the assumed parameters, the gas kinetic temperatures from Eq. (14) are 22, 54, 70, and 122 K for cosmic-ray ionization rates of 10^{-15}, 10^{-14}, 2×10^{-14}, and 10^{-13} s^{-1}. Thus, if cosmic rays play an important role in heating the gas, a cosmic-ray ionization rate of at least $1-2 \times 10^{-14}$ s^{-1} is required to explain the observed temperatures in the GC, which is about three orders of magnitude higher than in the solar neighborhood (e.g., Farquhar et al. 1994). Such an enhanced flux of cosmic-ray electrons is inferred in Sgr B2 by Yusef-Zadeh et al. (2007), and is interpreted as the main molecular-gas heating source in this region. The required high cosmic ray flux of $1-2 \times 10^{-14}$ s^{-1} would lead to an H I density of about 500 cm^{-3} (Güsten et al. 1981). Such a large H I abundance will cause noticeable 21 cm signals, which have indeed been seen in H I absorption surveys toward some GC clouds (e.g., Schwarz et al. 1977; Lang et al. 2010). For comparison, Bradford et al. (2003) estimate that a high supernova rate in the nucleus of NGC 253 results in a cosmic-ray ionization rate of $1.5-5.3 \times 10^{-14}$ s^{-1}. This mechanism may also play an important role in regulating the gas in ultraluminous infrared galaxies (ULIRGs) where the cosmic ray energy density may be as high as 1000 times that of the local Galactic value or even higher (Papadopoulos 2010; Papadopoulos et al. 2011).

4.4.3. Turbulent heating

The dissipation of turbulent kinetic energy provides a potentially important heating source in Galactic astrophysical environments, such as interstellar clouds (e.g., Falgarone & Puget 1995) and the warm ionized medium (e.g., Minter & Balser 1997), and in extragalactic environments, such as intracluster cooling flows (Dennis & Chandran 2005). The observed large velocity dispersion in the GC requires energy input to support the turbulence because the dynamic timescale is rather short, around 10^6 years. This implies a high turbulent heating rate. Following Pan & Padoan (2009), the turbulent heating rate is given by

$$\Gamma_{\rm turb} = n\,\mu\,m_{\rm H}\bar{\epsilon}, \tag{16}$$

where n and $m_{\rm H}$ are the number density and the mass of the hydrogen atom, μ is the mean molecular weight, $\mu = 2.35$ for molecular clouds, and $\bar{\epsilon}$ is the average dissipation rate per unit mass. The average dissipation rate per unit mass, is given by

$$\bar{\epsilon} = 0.5\,\sigma_{\rm v}^3/L, \tag{17}$$

where $\sigma_{\rm v}$ is the one-dimensional velocity dispersion and L the size of the cloud. Replacing the expression for $\bar{\epsilon}$ in Eq. (16) and substituting units, the average turbulent heating rate is

$$\bar{\Gamma}_{\rm turb} = 3.3 \times 10^{-27}\,n\,\sigma_{\rm v}^3\,L^{-1}\,{\rm erg\,cm}^{-3}\,{\rm s}^{-1}, \tag{18}$$

where the gas density n is in units of cm^{-3}, the one-dimensional velocity dispersion $\sigma_{\rm v}$ is in units of km s^{-1}, and the cloud size L is in units of pc. We can relate the one-dimensional velocity dispersion and the observed FWHM line widths by the conversion $\sigma_{\rm v} = V_{\rm FWHM}/2.355$ (Pan & Padoan 2009).

If turbulent heating dominates the heating process, the gas kinetic temperature can be estimated from thermal equilibrium

$$\bar{\Gamma}_{\rm turb} = \Lambda_{\rm g-d} + \Lambda_{\rm gas}. \tag{19}$$

To solve the equation above simply, we set the dust temperature to $T_{\rm d} = 0$ K, yielding a minimum $T_{\rm kin}$ value and its simple analytic solution as

$$T_{\rm kin} = \left(\frac{\left(16 \times 10^{-8}\,n^3 + 7920\,n^{0.5}\,{\rm d}v/{\rm d}r\,\sigma_{\rm v}^3\,L^{-1}\right)^{0.5}}{12\,{\rm d}v/{\rm d}r}\right.$$
$$\left. -\frac{4 \times 10^{-4}\,n^{1.5}}{12\,{\rm d}v/{\rm d}r}\right)^{2/3}. \tag{20}$$

Choosing a velocity gradient of 5 km s^{-1} pc^{-1}, an observed FWHM line width of 20 km s^{-1}, and a cloud size of 5 pc, the derived gas kinetic temperature ranges between 51 and 62 K for a range in gas density of 10^4 to 10^5 cm^{-3}.

For gas densities $n \le 10^5$ cm^{-3} and the assumed parameters as above, line cooling dominates the cooling process and the solution can be simplified to

$$T_{\rm kin} = 62 \left(\frac{n}{10^{4.5}\,{\rm cm}^{-3}}\right)^{1/6} \left(\frac{L}{5\,{\rm pc}}\,\frac{{\rm d}v/{\rm d}r}{5\,{\rm km\,s}^{-1}\,{\rm pc}^{-1}}\right)^{-1/3}$$
$$\times \left(\frac{V_{\rm FWHM}}{20\,{\rm km\,s}^{-1}}\right)\,{\rm K}. \tag{21}$$

This equation underestimates the gas temperature by less than 10% in comparison with Eq. (20), and shows that the temperature depends only weakly on the gas density, cloud size, and velocity gradient, but strongly depends on line width. Considering the line widths in different clouds, we can use Eq. (20) to calculate the temperatures and present the results in the last column of Table 1. To compare the calculated temperatures by turbulent heating with the ones derived from the H$_2$CO measurements in Sect. 4.3, we plot both temperatures in Fig. 7. In general, the temperatures agree within the uncertainties, supporting turbulent heating as a good candidate to heat the gas to the high temperatures observed in the GC. High gas kinetic temperatures were also deduced from NH$_3$ absorption lines toward Sgr B2 by Wilson et al. (1982). They suggested that the high gas temperatures were caused by turbulence maintained by shearing forces as a consequence of galactic rotation.

For turbulent and cosmic-ray heating, we cannot distinguish which mechanism dominates the heating of molecular clouds in the GC. With a large interferometer such as ALMA, one can try to search for molecular clumps with thermal line widths, i.e. with line widths that are dominated by thermal motion. If such objects can be found, turbulent heating can be excluded because the narrow line widths cannot be explained by turbulent heating, and the cosmic-ray heating will then be the dominant process to heat the gas to high temperatures. Future observations of $x(e) = \frac{n_e}{2n_{\rm H_2}}$ (the average ionization fraction) can also help distinguish between these two heating mechanisms, because high cosmic-ray energy densities will boost this fraction, unlike turbulence (Papadopoulos 2010 and references therein).

The special thermal state of the GC clouds may be the average state of the molecular ISM in ULIRGs, with a direct impact
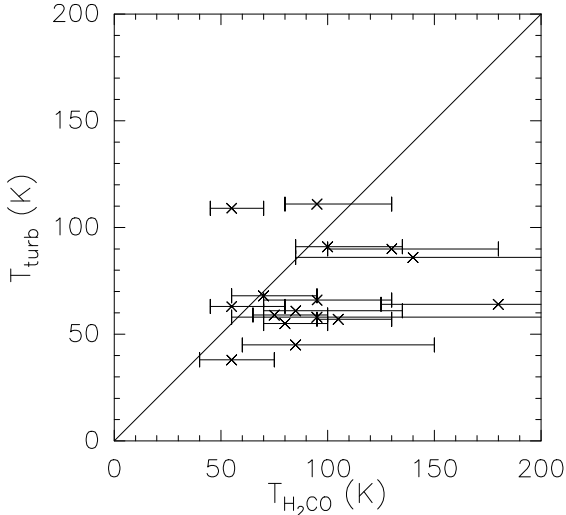
Fig. 7. Gas temperatures estimated by turbulent heating versus those derived from the H$_2$CO LVG models with [para-H$_2$CO] = 10^{-10}. The solid line shows the relationship for the cases where both temperatures are the same.

on their stellar IMF (Papadopoulos et al. 2011). The high temperatures of molecular clouds on large scales in the GC region may be driven by turbulent energy dissipation and/or cosmic-rays instead of photons. Such a non-photon-driven thermal state of the molecular gas provides an excellent template for studying the intial conditions and star formation for the galaxy-sized gas in ULIRGs.

5. Conclusions

The $J_{K_a K_c} = 3_{03} \rightarrow 2_{02}$, $3_{22} \rightarrow 2_{21}$, and $3_{21} \rightarrow 2_{20}$ transitions of para-H$_2$CO were observed simultaneously with the APEX telescope, covering an area of roughly $40' \times 8'$ along the Galactic plane with a linear resolution of 1.2 pc, including the Galactic center. The main results from these measurements follow.

(1) The strongest line of the 218 GHz H$_2$CO triplet, H$_2$CO ($3_{03} \rightarrow 2_{02}$), is widespread in the mapped region, and its emission shows a morphology similar to ammonia (Güsten et al. 1981).

(2) The para-H$_2$CO abundance is found to be $0.5-1.2 \times 10^{-9}$, which is consistent with previous studies of formaldehyde absorption lines at cm-wavelengths in the Galactic center region.

(3) Using LVG models, we can constrain gas kinetic temperatures to be of about 85 K for the Galactic center clouds, ranging from 50 to values above 100 K. While a systematic trend of (decreasing) kinetic temperature versus (increasing) angular distance from the nucleus is not found, the clouds with highest temperature ($T_{kin} > 100$ K) are all located near the center. Molecular gas outside of the dense cores in the Galactic center region is characterized by a gas kinetic temperature of 65 ± 10 K.

(4) The high temperatures found in the Galactic center region may be caused by turbulent heating and/or cosmic-ray heating. Turbulent heating can readily heat the gas to the values deduced from H$_2$CO. If cosmic-ray heating dominates the heating process, a cosmic-ray ionization rate of at least $1-2 \times 10^{-14}$ is required to explain the observed temperatures. The high temperatures of molecular clouds on large scales in the Galactic center region may be driven by turbulent energy dissipation and/or cosmic-rays instead of photons. Such a non-photon-driven thermal state of the molecular gas make such clouds excellent templates for the starbursts found in ultraluminous infrared galaxies.

References

Alexander, R. D., Begelman, M. C., & Armitage, P. J. 2007, ApJ, 654, 907
Amo-Baladrón, M. A., Martín-Pintado, J., Morris, M. R., Muno, M. P., & Rodríguez-Fernández, N. J. 2009, ApJ, 694, 943
Arons, J., & Max, C. E. 1975, ApJ, 196, L77
Bally, J., Stark, A. A., Wilson, R. W., & Henkel, C. 1987, ApJS, 65, 13
Bartko, H., Martins, F., Trippe, S., et al. 2010, ApJ, 708, 834
Bradford, C. M., Nikola, T., Stacey, G. J., et al. 2003, ApJ, 586, 891
Caselli, P., Hasegawa, T. I., & Herbst, E. 1993, ApJ, 408, 548
Croker, P. M., Jones, D. L., Melia, F., Ott, J., & Protheroe, R. J. 2010, Nature, 463, 65
Dahmen, G., Hüttemeister, S., Wilson, T. L., & Mauersberger, R. 1998, A&A, 331, 959
Dame, T. M. 2011, [arXiv:1101.1499]
Dame, T. M., Ungerechts, H., Cohen, R. S., et al. 1987, ApJ, 322, 706
Dame, T. M., Hartmann, D., & Thaddeus, P. 2001, ApJ, 547, 792
Danby, G., Flower, D. R., Valiron, P., Schilke, P., & Walmsley, C. M. 1988, MNRAS, 235, 229
Dennis, T. J., & Chandran, B. D. G. 2005, ApJ, 622, 205
Dogiel, V. A., Cheng, K.-S., Chernyshov, D. O., et al. 2011, in The Galactic Center: a Window to the Nuclear Environment of Disk Galaxies, eds. M. R. Morris, Q. D. Wang, & F. Yuan (San Francisco: ASP), 426
Eckart, A., García-Marín, M., Vogel, S. N., et al. 2012, A&A, 537, A52
Falgarone, E., & Puget, J.-L. 1995, A&A, 293, 840
Farquhar, P. R. A., Millar, T. J., & Herbst, E. 1994, MNRAS, 269, 641
Ferriére, K. 2009, A&A, 505, 1183
García-Marín, M., Eckart, A., Weiss, A., et al. 2011, ApJ, 738, 158
Goldsmith, P. F., & Langer, W. D. 1978, ApJ, 222, 881
Green, S. 1991, ApJS, 76, 979
Güsten, R., & Henkel, C. 1983, A&A, 125, 136
Güsten, R., & Philipp, S. D. 2004, The Dense Interstellar Medium in Galaxies, 253
Güsten, R., Walmsley, C. M., & Pauls, T. 1981, A&A, 103, 197
Güsten, R., Henkel, C., & Batrla, W. 1985a, A&A, 149, 195
Güsten, R., Walmsley, C. M., Ungerechts, H., & Churchwell, E. 1985b, A&A, 142, 381
Güsten, R., Nyman, L. Å., Schilke, P., et al. 2006, A&A, 454, L13
Hollenbach, D. J., & Tielens, A. G. G. M. 1999, Rev. Mod. Phys., 71, 173
Hüttemeister, S., Dahmen, G., Mauersberger, R., et al. 1998, A&A, 334, 646
Hüttemeister, S., Wilson, T. L., Bania, T. M., & Martin-Pintado, J. 1993, A&A, 280, 255
Johnstone, D., Boonman, A. M. S., & van Dishoeck, E. F. 2003, A&A, 412, 157
Jones, P. A., Burton, M. G., Cunningham, M. R., et al. 2012, MNRAS, 419, 2961
Kim, S., Martin, C. L., Stark, A. A., & Lane, A. P. 2002, ApJ, 580, 896
Klein, B., Philipp, S. D., Krämer, I., et al. 2006, A&A, 454, L29
Klessen, R. S., Spaans, M., & Jappsen, A.-K. 2007, MNRAS, 374, L29
Koyama, K., Hyodo, Y., Inui, T., et al. 2007, PASJ, 59, 245
Krügel, E., & Walmsley, C. M. 1984, A&A, 130, 5
Lang, C. C., Goss, W. M., Cyganowski, C., & Clubb, K. I. 2010, ApJS, 191, 275
Mühle, S., Seaquist, E. R., & Henkel, C. 2007, ApJ, 671, 1579
Maloney, P. R., Hollenbach, D. J., & Tielens, A. G. G. M. 1996, ApJ, 466, 561
Mangum, J. G., & Wootten, A. 1993a, ApJS, 89, 123
Mangum, J. G., Wootten, A., & Plambeck, R. L. 1993b, ApJ, 409, 282
Martin-Pintado, J., de Vicente, P., Fuente, A., & Planesas, P. 1997, ApJ, 482, L45
Mauersberger, R., Henkel, C., Weiß, A., Peck, A. B., & Hagiwara, Y. 2003, A&A, 403, 561
Mauersberger, R., Henkel, C., Wilson, T. L., & Walmsley, C. M. 1986, A&A, 162, 199
Mauersberger, R., Henkel, C., & Wilson, T. L. 1987, A&A, 173, 352
Minter, A. H., & Balser, D. S. 1997, ApJ, 484, L133
Molinari, S., Bally, J., Noriega-Crespo, A., et al. 2011, ApJ, 735, L33
Morris, M., & Serabyn, E. 1996, ARA&A, 34, 645

Mundy, L. G., Evans, N. J., II, Snell, R. L., & Goldsmith, P. F. 1987, ApJ, 318, 392

Muno, M. P., Baganoff, F. K., Bautz, M. W., et al. 2004, ApJ, 613, 326

Myers, P. C., & Benson, P. J. 1983, ApJ, 266, 309

Nagai, M., Tanaka, K., Kamegai, K., & Oka, T. 2007, PASJ, 59, 25

Nowak, M. A., Neilsen, J., Markoff, S. B., et al. 2012, ApJ, 759, 95

Nummelin, A., Bergman, P., Hjalmarson, Å., et al. 2000, ApJS, 128, 213

Nummelin, A., Bergman, P., Hjalmarson, A., et al. 1998, ApJS, 117, 427

Oka, T., Nagai, M., Kamegai, K., & Tanaka, K. 2011, ApJ, 732, 120

Pan, L., & Padoan, P. 2009, ApJ, 692, 594

Papadopoulos, P. P. 2010, ApJ, 720, 226

Papadopoulos, P. P., Thi, W.-F., Miniati, F., & Viti, S. 2011, MNRAS, 414, 1705

Pierce-Price, D., Richer, J. S., Greaves, J. S., et al. 2000, ApJ, 545, L121

Reid, M. J. 1993, ARA&A, 31, 345

Requena-Torres, M. A., Martín-Pintado, J., Rodríguez-Franco, A., et al. 2006, A&A, 455, 971

Rodríguez-Fernández, N. J., Martín-Pintado, J., Fuente, A., & Wilson, T. L. 2004, A&A, 427, 217

Scalo, J. M. 1977, ApJ, 213, 705

Schulz, A., Güsten, R., Köster, B., & Krause, D. 2001, A&A, 371, 25

Schwarz, U. J., Shaver, P. A., & Ekers, R. D. 1977, A&A, 54, 863

Tielens, A. G. G. M. (ed.) 2005, The Physics and Chemistry of the Interstellar Medium (Cambridge: Cambridge Univ. Press)

Walmsley, C. M., & Ungerechts, H. 1983, A&A, 122, 164

Weiß, A., Neininger, N., Henkel, C., Stutzki, J., & Klein, U. 2001, ApJ, 554, L143

Wilson, T. L., Ruf, K., Walmsley, C. M., et al. 1982, A&A, 115, 185

Wootten, A., Evans, N. J., II, Snell, R., & vanden Bout, P. 1978, ApJ, 225, L143

Yuasa, T., Tamura, K.-I., Nakazawa, K., et al. 2008, PASJ, 60, 207

Yusef-Zadeh, F., Wardle, M., & Roy, S. 2007, ApJ, 665, L123

Zylka, R., Güsten, R., Henkel, C., & Batrla, W. 1992, A&AS, 96, 525

Appendix A: H_2CO line parameters

Table A.1. Line parameters.

Position				T_{mb}	V_{LSR}	$\Delta V_{1/2}$	$\int T_{mb}dv$
	(arcsec, arcsec)			(K)	($km\,s^{-1}$)	($km\,s^{-1}$)	($K\,km\,s^{-1}$)
P 1	−75	−390	$H_2CO\ 3_{03} \to 2_{02}$	0.75(0.04)	2.9(0.4)	35.4(1.1)	26.4(0.7)
			$H_2CO\ 3_{22} \to 2_{21}$	0.13(0.03)	8.0(2.6)	39.8(6.4)	5.1(0.7)
			$H_2CO\ 3_{21} \to 2_{20}$	0.19(0.03)	2.5(1.2)	38.3(3.2)	7.3(0.5)
P 2	−60	−330	$H_2CO\ 3_{03} \to 2_{02}$	1.95(0.05)	6.5(0.2)	18.8(0.4)	36.7(0.7)
			$H_2CO\ 3_{22} \to 2_{21}$	0.72(0.04)	7.1(0.3)	13.1(0.8)	9.5(0.5)
			$H_2CO\ 3_{21} \to 2_{20}$	0.65(0.03)	6.7(0.2)	14.3(0.7)	9.5(0.3)
P 3	−30	−210	$H_2CO\ 3_{03} \to 2_{02}$	2.64(0.04)	16.4(0.1)	19.4(0.2)	51.2(0.5)
			$H_2CO\ 3_{22} \to 2_{21}$	0.83(0.03)	18.4(0.2)	18.0(0.4)	15.0(0.3)
			$H_2CO\ 3_{21} \to 2_{20}$	0.76(0.02)	17.7(0.2)	17.7(0.4)	13.5(0.2)
P 4	30	−60	$H_2CO\ 3_{03} \to 2_{02}$	0.83(0.02)	33.2(0.2)	20.1(0.5)	16.7(0.3)
			$H_2CO\ 3_{22} \to 2_{21}$	0.21(0.01)	34.0(0.4)	19.5(1.4)	4.2(0.2)
			$H_2CO\ 3_{21} \to 2_{20}$	0.21(0.01)	33.5(0.3)	16.1(1.0)	3.4(0.1)
P 6	135	0	$H_2CO\ 3_{03} \to 2_{02}$	1.08(0.04)	46.2(0.3)	30.2(0.7)	32.7(0.7)
			$H_2CO\ 3_{22} \to 2_{21}$	0.37(0.03)	44.6(0.6)	26.0(1.3)	9.6(0.4)
			$H_2CO\ 3_{21} \to 2_{20}$	0.41(0.02)	44.2(0.4)	24.4(0.9)	10.2(0.3)
P 7	195	75	$H_2CO\ 3_{03} \to 2_{02}$	1.23(0.04)	40.2(0.3)	36.8(0.6)	45.0(0.7)
			$H_2CO\ 3_{22} \to 2_{21}$	0.40(0.02)	37.3(0.6)	31.5(1.4)	12.7(0.5)
			$H_2CO\ 3_{21} \to 2_{20}$	0.36(0.02)	39.8(0.4)	34.9(1.0)	12.4(0.3)
P 8	135	90	$H_2CO\ 3_{03} \to 2_{02}$	2.07(0.07)	47.0(0.3)	27.4(0.6)	56.5(1.1)
			$H_2CO\ 3_{22} \to 2_{21}$	0.85(0.03)	48.2(0.2)	26.0(0.6)	22.2(0.4)
			$H_2CO\ 3_{21} \to 2_{20}$	0.81(0.02)	47.5(0.2)	23.0(0.4)	18.6(0.3)
P 9	60	120	$H_2CO\ 3_{03} \to 2_{02}$	0.60(0.02)	49.3(0.3)	28.6(0.6)	17.3(0.3)
			$H_2CO\ 3_{22} \to 2_{21}$	0.16(0.02)	49.3(...)[a]	38.2(4.6)	5.9(0.8)
			$H_2CO\ 3_{21} \to 2_{20}$	0.17(0.01)	48.5(0.7)	28.9(1.7)	4.8(0.2)
P 9	60	120	$H_2CO\ 3_{03} \to 2_{02}$	0.37(0.02)	−4.2(0.4)	19.8(0.9)	7.3(0.3)
			$H_2CO\ 3_{22} \to 2_{21}$	0.12(0.02)	−4.2(...)[a]	16.9(2.3)	2.1(0.3)
			$H_2CO\ 3_{21} \to 2_{20}$	0.11(0.01)	−4.7(0.9)	20.2(2.0)	2.1(0.2)
P10	90	135	$H_2CO\ 3_{03} \to 2_{02}$	1.07(0.04)	55.5(0.2)	30.0(0.6)	31.9(0.5)
			$H_2CO\ 3_{22} \to 2_{21}$	0.32(0.02)	54.8(0.6)	31.4(1.6)	10.2(0.4)
			$H_2CO\ 3_{21} \to 2_{20}$	0.29(0.02)	55.0(0.4)	30.1(1.1)	8.8(0.3)
P12	150	225	$H_2CO\ 3_{03} \to 2_{02}$	0.56(0.03)	44.4(0.3)	21.5(0.9)	12.2(0.4)
			$H_2CO\ 3_{22} \to 2_{21}$	0.20(0.03)	44.4(...)[a]	18.3(2.4)	3.8(0.5)
			$H_2CO\ 3_{21} \to 2_{20}$	0.12(0.02)	42.4(1.3)	19.8(2.9)	2.3(0.3)
P12	150	225	$H_2CO\ 3_{03} \to 2_{02}$	0.72(0.03)	−10.9(0.2)	15.7(0.5)	11.4(0.3)
			$H_2CO\ 3_{22} \to 2_{21}$	0.29(0.03)	−10.9(...)[a]	13.5(1.2)	3.9(0.3)
			$H_2CO\ 3_{21} \to 2_{20}$	0.25(0.02)	−10.6(0.4)	11.4(1.3)	2.9(0.3)
P13	315	315	$H_2CO\ 3_{03} \to 2_{02}$	1.41(0.05)	51.3(0.2)	22.3(0.5)	31.5(0.7)
			$H_2CO\ 3_{22} \to 2_{21}$	0.41(0.04)	52.2(0.7)	21.1(1.8)	8.7(0.6)
			$H_2CO\ 3_{21} \to 2_{20}$	0.40(0.03)	51.5(0.5)	21.5(1.2)	8.7(0.4)
P14	165	330	$H_2CO\ 3_{03} \to 2_{02}$	0.99(0.04)	46.7(0.2)	13.6(0.5)	13.5(0.4)
			$H_2CO\ 3_{22} \to 2_{21}$	0.20(0.03)	45.9(1.0)	12.5(3.2)	2.5(0.4)
			$H_2CO\ 3_{21} \to 2_{20}$	0.28(0.03)	46.7(0.5)	12.7(1.2)	3.6(0.3)
P15	420	435	$H_2CO\ 3_{03} \to 2_{02}$	1.83(0.06)	52.9(0.2)	21.8(0.5)	39.9(0.7)
			$H_2CO\ 3_{22} \to 2_{21}$	0.68(0.04)	52.7(0.3)	19.6(0.8)	13.4(0.5)
			$H_2CO\ 3_{21} \to 2_{20}$	0.65(0.02)	52.5(0.2)	19.5(0.6)	12.8(0.3)
P16	165	570	$H_2CO\ 3_{03} \to 2_{02}$	1.09(0.05)	51.0(0.3)	20.9(0.7)	22.8(0.7)
			$H_2CO\ 3_{22} \to 2_{21}$	0.33(0.04)	50.7(0.7)	18.9(2.1)	6.3(0.5)
			$H_2CO\ 3_{21} \to 2_{20}$	0.36(0.04)	50.3(0.6)	16.5(1.4)	5.9(0.4)
P22	390	1020	$H_2CO\ 3_{03} \to 2_{02}$	1.15(0.06)	35.7(0.3)	22.9(0.8)	26.1(0.8)
			$H_2CO\ 3_{22} \to 2_{21}$	0.37(0.04)	35.4(0.6)	16.2(1.7)	6.2(0.5)
			$H_2CO\ 3_{21} \to 2_{20}$	0.36(0.04)	35.8(0.6)	18.2(1.5)	6.7(0.5)

Notes. [a] To obtain Gaussian fits of the $H_2CO\ 3_{22} \to 2_{21}$ transition at locations with two velocity components, we adopt the same central velocities as determined for the $H_2CO\ 3_{03} \to 2_{02}$ transition.

Appendix B

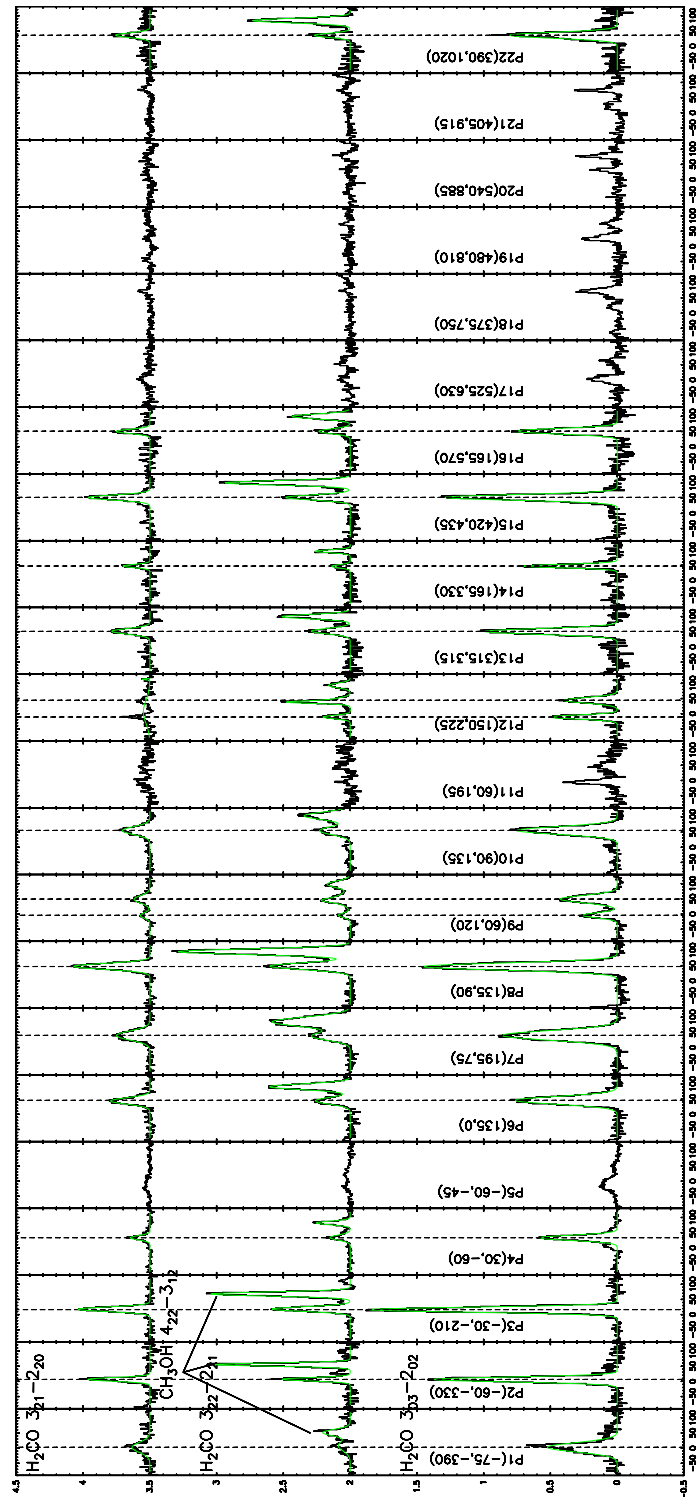### B.1. H_2CO spectral lines

Fig. B.1. Spectra of different positions marked by the numbers in Fig. 2. All transitions from a given position are presented in the same panel but with different offsets along the y-axis on a T_A^* scale. The Gaussian fits are indicated with green lines, and the central velocities of the components are shown as dashed vertical lines.
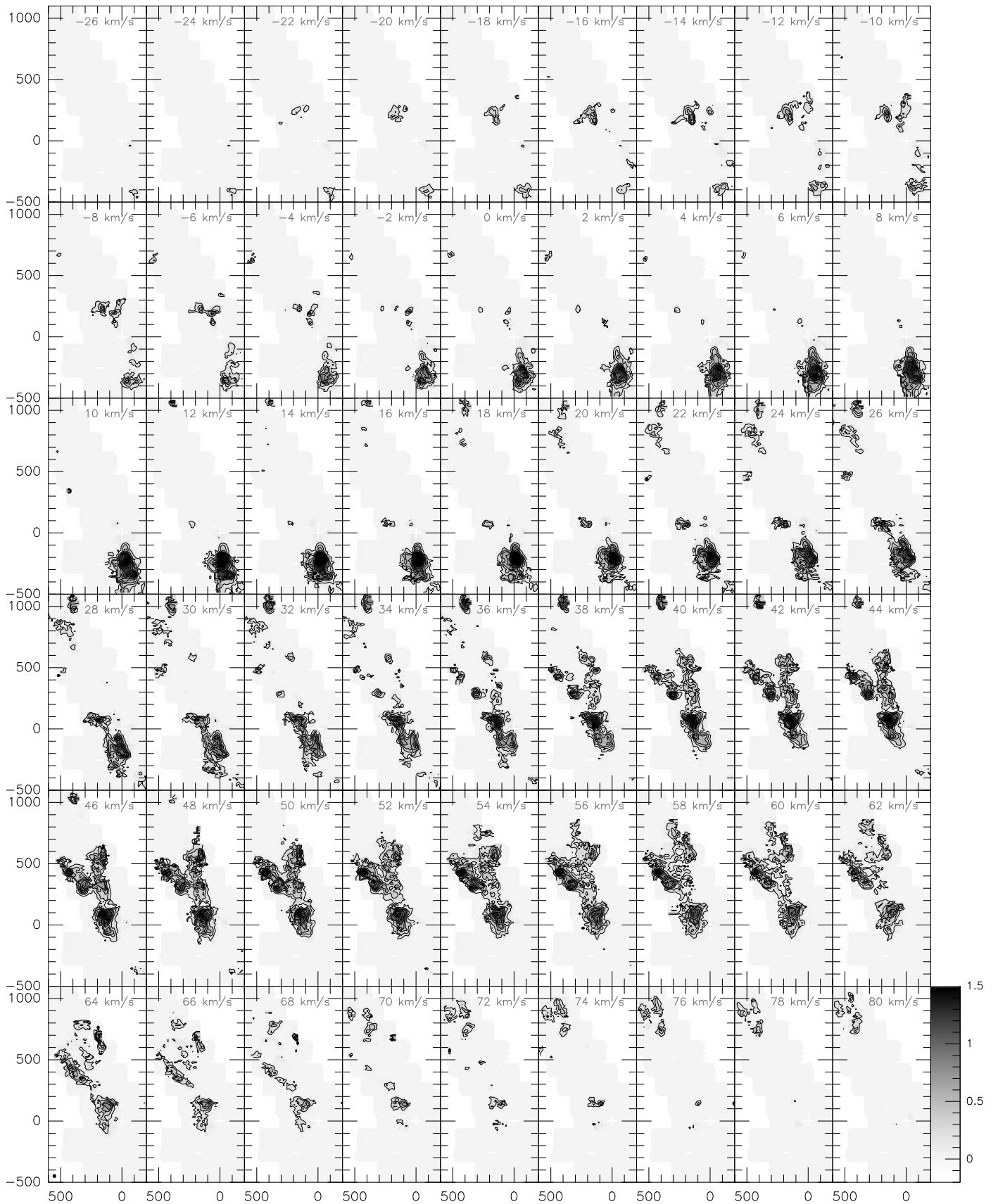
B.2. Velocity channel maps

Fig. B.2. Channel maps of the $H_2CO\ 3_{03} - 2_{02}$ emission. Black contour levels for the molecular line emission (on a T_A^* scale) are from 0.16 K (2σ) in s.pdf of 0.16 K. Velocity channels range from -27 to $+81$ km s^{-1} in s.pdf of 2 km s^{-1}. The central velocities of the channel maps are shown at the top of each panel. The wedge at the side shows the intensity scale of the line emission. The beam size of 30$''$ is shown in the bottom-left corner.
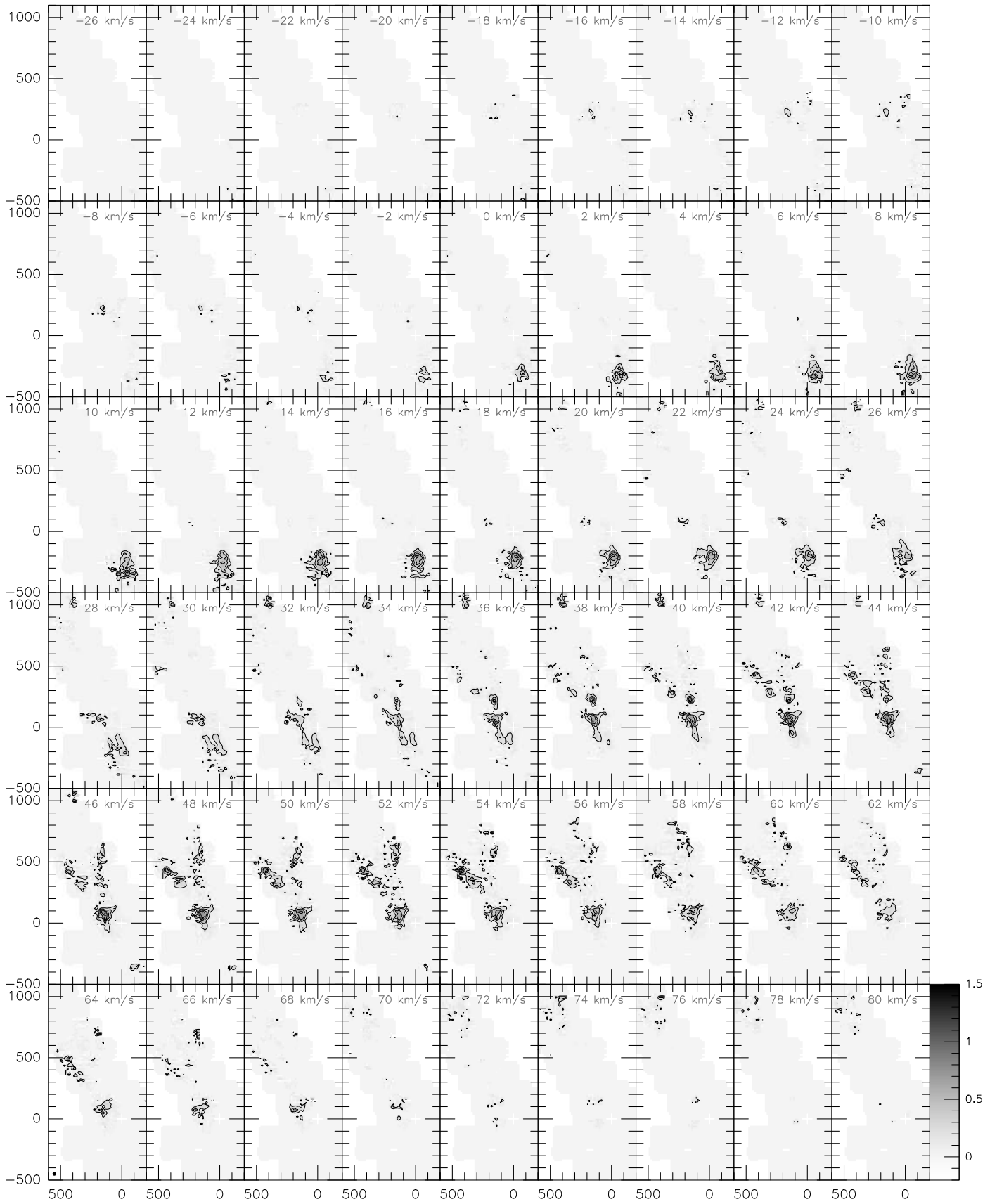
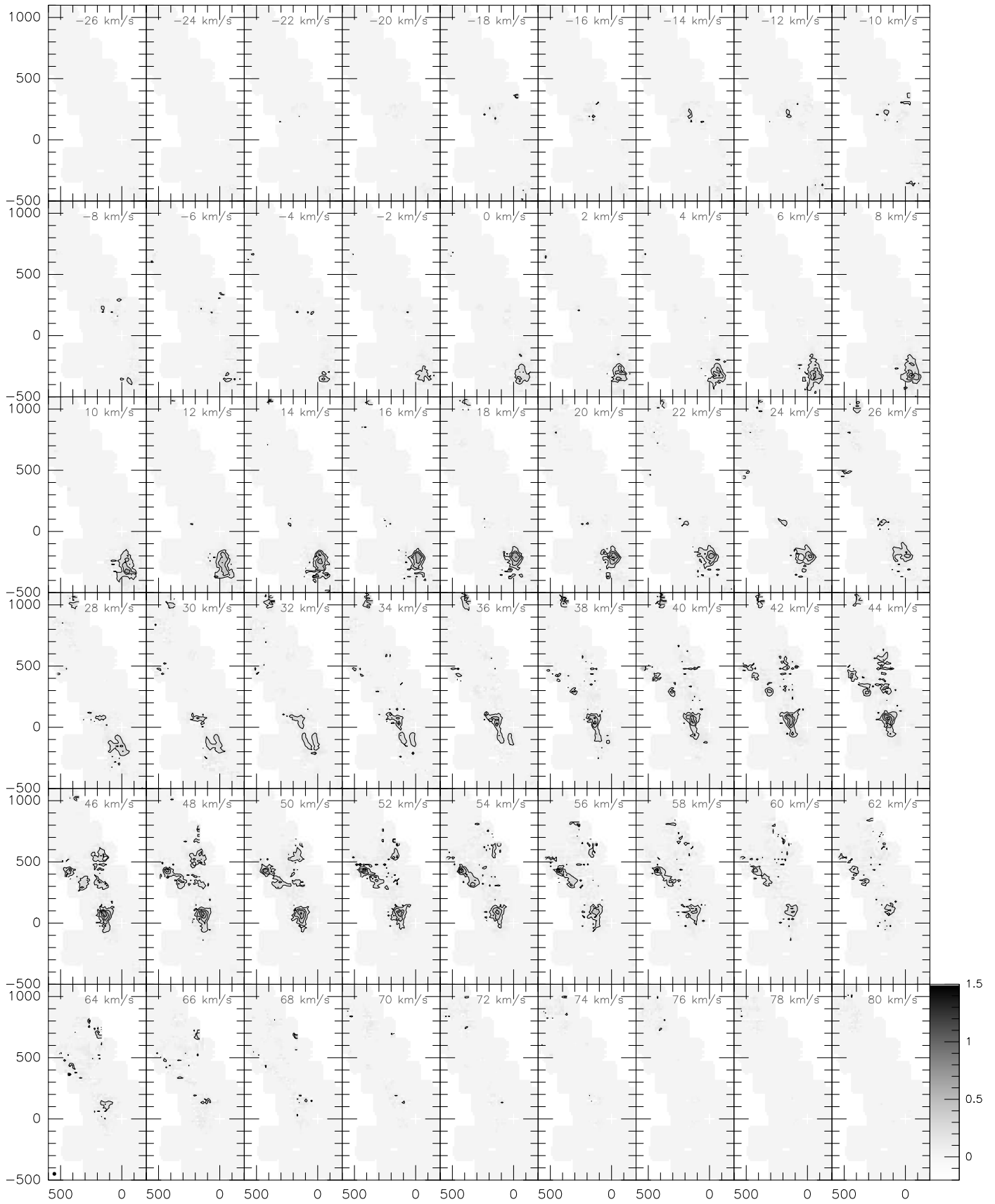**Fig. B.3.** Same as Fig. B.2 but for the H$_2$CO 3_{22}−2_{21} emission.

Fig. B.4. Same as Fig. B.2 but for the H_2CO $3_{21}-2_{20}$ emission.